이 학 석 사 학 위 논 문

Synthesis of Gold and Platinum Nanoparticles in Aqueous Solution Using a Redox Active Metal-Organic Framework

2013년 8월

서울대학교 대학원

화학부 무기화학 전공

전승안

Synthesis of Gold and Platinum Nanoparticles in Aqueous Solution Using a Redox Active Metal-Organic Framework

By

Seung-An Chyun

Supervisor: Prof. Myunghyun Paik Suh

A Thesis for the M.S. Degree

in Inorganic Chemistry

Department of Chemistry

Graduate School

Seoul National University

August, 2013

이 학 석 사 학 위 논 문

Synthesis of Gold and Platinum Nanoparticles in Aqueous Solution Using a Redox Active Metal-Organic Framework

지도교수 백 명 현

이 논문을 이학석사학위논문으로 제출함

2013년 6월

서울대학교 대학원

화학부 무기화학 전공

전승안

전승안의 석사학위 논문을 인준함

2013년 8월

위 원 장 _____ (인)

부 위 원 장 _____ (인)

위 원 _____ (인)

Abstract

Shaped gold nanoparticles (triangular, square, hexagonal shapes with size 20-75 nm; circular shape with size 5-15 nm) and platinum nanoparticles (circular shape with size 1.8-2.5 nm) have been fabricated by the simple immersion of a redox active coordination polymer or metal organic framework (**SNU-M55**) in the aqueous solutions of $NaAuCl_4 \cdot 6H_2O$ and K_2PtCl_4, respectively, without the assistance of an external mediator. **SNU-M55**, which is constructed using a light sensitizing $Ru(bpy)_3^{2+}$ moiety, a bismacrocyclic Ni(II) complex, and a dicarboxylate ligand, is shown to have previously unprecendented redox capabilities, capable of synthesizing platinum nanoparticles via simple immersion in the metal precursor, which has never been reported. Although the catalytic activity of the composite material was tested, no significant results were obtained.

Table of Contents

I.1. Introduction

Metal organic frameworks (MOFs) or porous coordination polymers (PCPs) are a class of crystalline materials which have gained great attention in the past few decades. They are synthesized using an inorganic 'joint' which is linked together by organic ligands which act as 'struts', extending into extended network structures.[1] MOFs are generally characterized by their porous structures and large internal surface areas exceeding 6 000 m^2/g.[2] By carefully designing the metal and organic building blocks incorporated in the structure, the properties of the MOFs can be tuned to possess a desired functionality that can be applied to gas storage and separation, ion-exchange, heterogeneous catalysis, sensor technology, and nanoparticle fabrication.[1]

I.1.1. Construction of Porous Metal-Organic Frameworks

The earliest example of MOFs were reported by Robson et al in 1989, and has since burgeoned into one of the fastest growing fields of research in chemistry.[3, 4] One of the primary reasons of this unparalleled growth is the facile synthetic route employed to create MOFs. MOFs are generally synthesized via self-assembly or solvothermal methods. By combining an organic building block with an inorganic salt MOFs are easily made. Although a wide variety of ligands have been used, the most common organic linkers include a carboxylate moiety that coordinates strongly to a metal center. Some examples of previously reported ligands can be seen in Figure 1.[5] The rigid metal-organic carbon clusters formed by the organic linker and metal ion with points of extension defining a geometrical shape is referred to as a secondary building unit (SBU).[6] The most representative example is

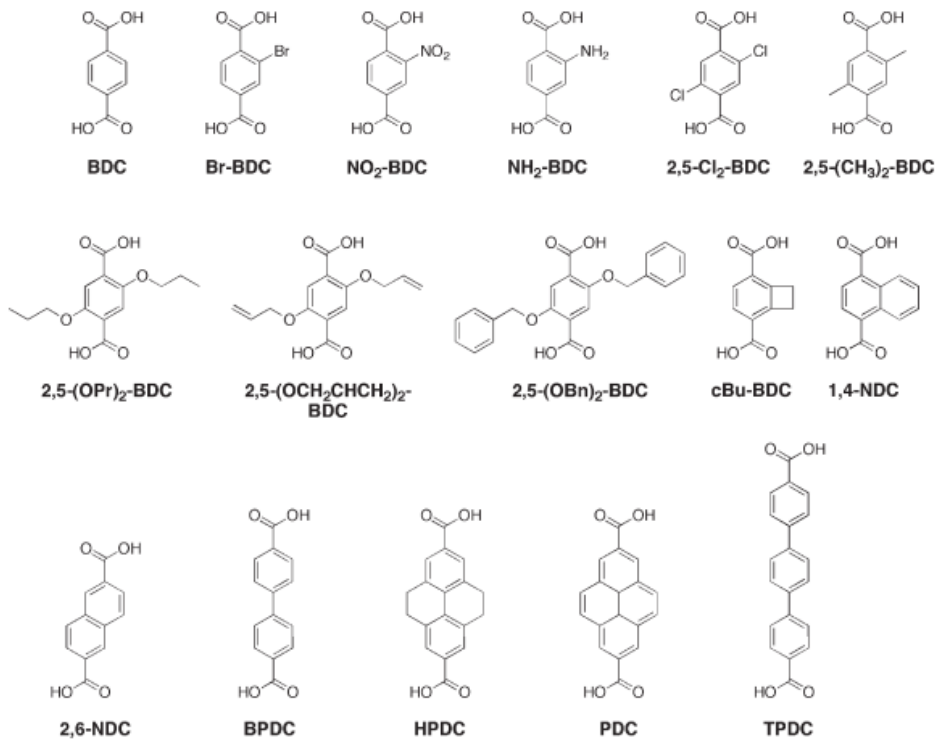

Figure 1. Various carboxylic acids used in the successful synthesis of MOFs.[5]

$[Zn_4O(BDC)_3]$•8DMF•C_6H_5Cl, also known as MOF-5 which was first reported by Yaghi *et al* in 1999.[7] This extremely robust framework has a cubic network in which the vertices are octahedral SBUs ($Zn_4O(CO_2)_6$) and the edges are benzene struts as seen in Figure 2. In addition to the octahedral SBU generated by MOF-5, other discrete SBUs have also been observed (triangles, squares, tetrahedral, etc.). The structure of the synthesized frameworks is largely dependent on the metal ion and organic linker employed, and the characterization of the resulting network topologies and structures have been thoroughly investigated. Similar analogues of MOF-5 were also synthesized by using rigid linear dicarboxylate ligands such as NDC, BPDC, PDC and TPDC.[8] MOFs have also been generated using

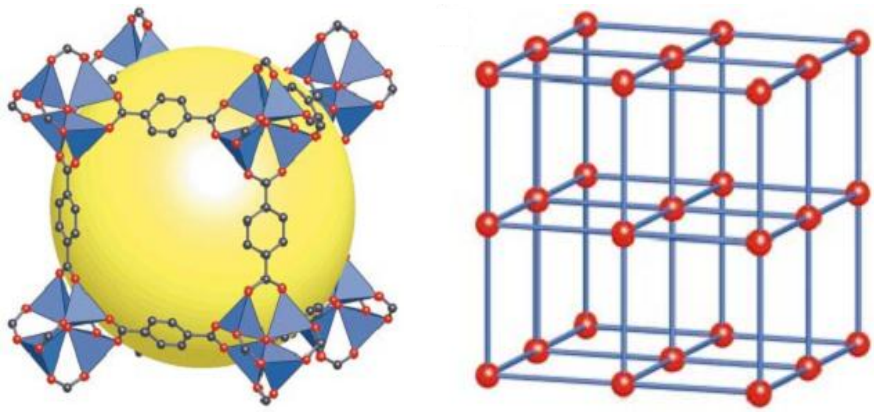

Figure 2. The bonding of the octahedral $Zn_4O(CO_2)_6$ unit joined with the organic benzene dicarboxylate linker to form a cubic network in MOF-5.[6]

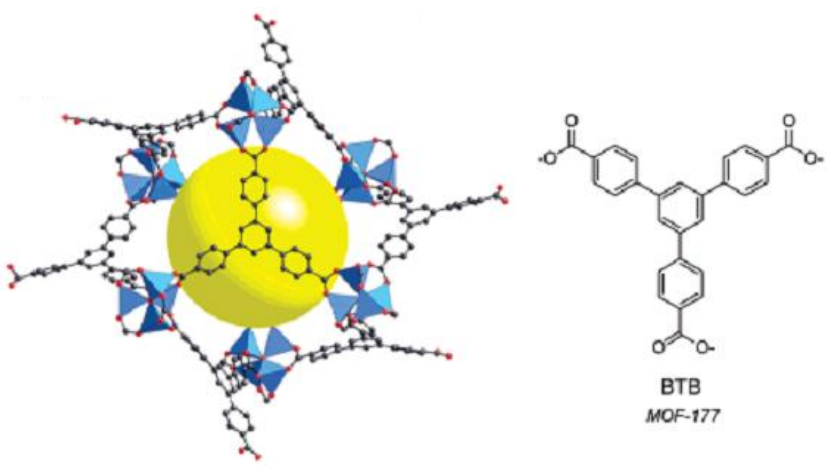

Figure 3. The bonding of three octahedral $Zn_4O(CO_2)_6$ unit to a single trigonal 1,3,5-benzentribenzoate ligand to form MOF-177.[9]

tricarboxylate linkers such as BTB which resulted in $[Zn_4O(BTB)_2]$•15DEF•$3H_2O$, or MOF-177 (Figure 3).[10] While the most common metal ions used are zinc and copper, there have been reports of various other metals such as niobium, zirconium, cobalt, iron, and titanium.[11] Some of these SBUs are shown in Figure 4.[12] Therefore, by judicious selection of the incorporated organic linker in the framework, pore size, surface area and other properties can be adjusted as desired.

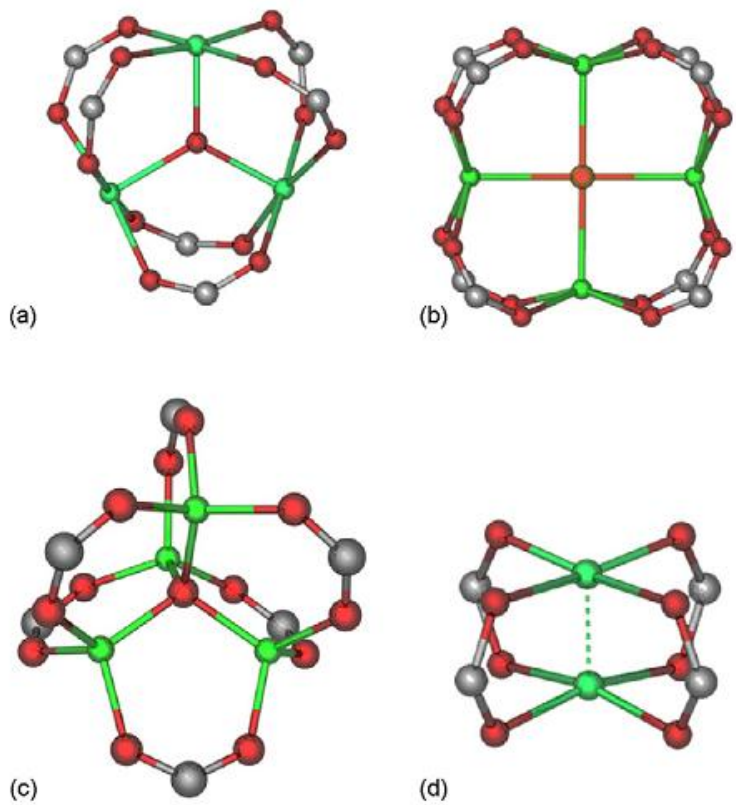

Figure 4. Some of the common SBUs formed from various metal ions in MOFs including (a) trigonal planar, (b) square planar, (c) tetrahedral, and (d) tetrahedral paddlewheel. [13]

I.1.1.2. Macrocyclic Based Metal-Organic Frameworks

In addition to the organic ligand, the inorganic 'joint' also offers an opportunity to direct the geometry of the resulting framework. One example is the use of macrocyclic complexes, which was pioneered by the Suh Group. Macrocyclic building blocks have several advantages over free metal ions. Free metal ions offer limited control in the extending direction of the network due to the multiple coordination sites. In contrast, square planar macrocyclic metal complexes only have two vacant coordination sites found at the axial position. This greatly simplifies the design and prediction of the resulting network. For example, if the trigonal organic building block, 1,3,5-benzenetricarboxylate (BTC^{3-}) is assembled with a nickel based macrocyclic complex, a honeycomb or brick-wall framework can be constructed, based on the solvent used during self-assembly, as seen in Figure 5.[14]

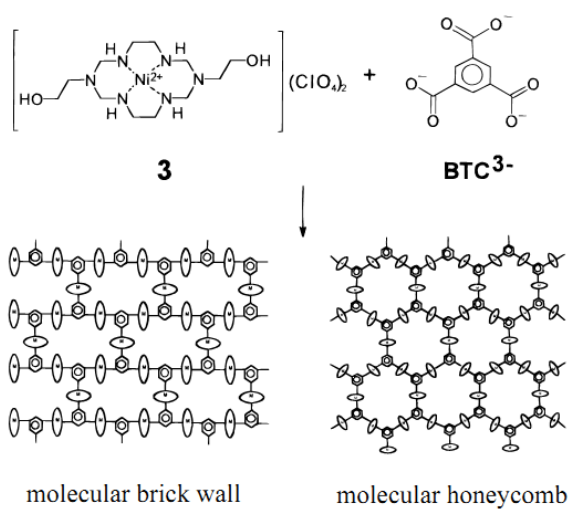

Figure 5. The resulting framework from the self-assembly of a nickel based macrocycle and a trigonal based building block.

Further studies also revealed that monomacrocyclic complexes assembled with square planar organic building blocks result in 2D layer networks. However, when bismacrocyclic complexes are used, the organic bridge between the two macrocycles connects two discrete 2D layers, resulting in a bilayer type structure or a 3D multilayered type structure. Some examples of macrocyclic complexes used in the synthesis of MOFs can be found in Figure 6.[15]

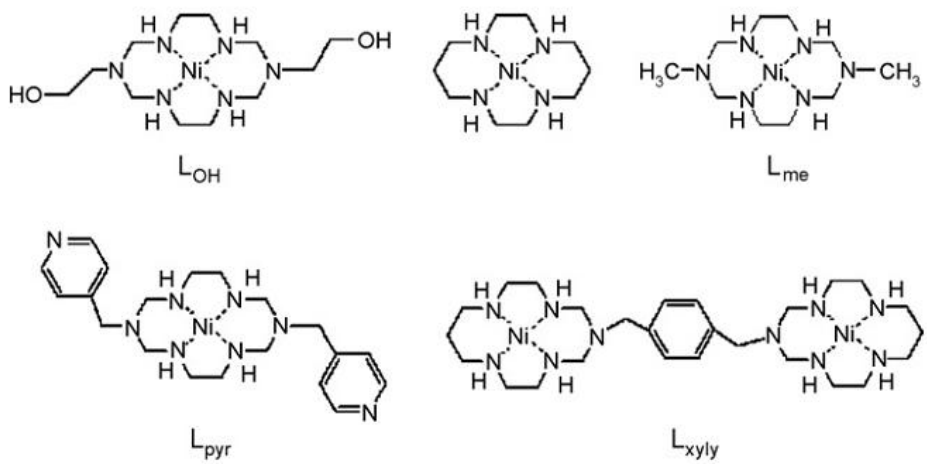

Figure 6. Some examples of Ni(II) macrocyclic complexes used in the synthesis of MOFs.[15]

I.2. A Brief Overview of Applications

Since the proliferation of this field of chemistry, the applications of these robust materials seem to be limited only by the imagination. Due to the porous nature of MOFs, they first began as gas storage and separation materials but as the field has evolved, researchers have begun to discover a multitude of other applications. In addition to gas storage and separation, MOFs have been used for ion exchange, heterogeneous catalysis, sensor technology, and nanoparticle fabrication.[1] This section will briefly cover three of these topics.

I.2.1 Gas Storage and Separation

One of the most widely studied applications of this new class of materials is gas storage and separation. The porous nature of MOFs makes them extremely attractive candidates for this type of application and hundreds of papers have been published studying this particular property. Perhaps the two most intensively studied gas interactions are carbon dioxide and hydrogen.

I.2.1.1 Carbon Dioxide Capture

Due to the implication of carbon dioxide's correlation with global warming, great efforts have been made to reduce carbon dioxide emissions from industrial sources. Currently, 80% of CO_2 emissions from anthropogenic sources originate from the combustion of coal, oil, and natural gas. With these levels projected to rise in the future, it would be worthwhile to develop technologies capable of capturing carbon dioxide from existing emission sources. MOFs have shown great promise in this area, capable of adsorbing large amounts of carbon dioxide. Some of the factors that are important to consider when considering MOFs as a CO_2 capture material include the adsorption capacity, enthalpy of adsorption, and selectivity over other gases. [16]

The adsorption, or uptake capacity, is evaluated in two ways: *gravimetric* CO_2 uptake, and *volumetric* capacity. The gravimetric uptake capacity refers to the quantity of CO_2 adsorbed within a unit mass of the material. The volumetric capacity on the other hand refers to how densely the CO_2 can be stored within the material. These two parameters are generally determined by absolute adsorption

isotherms. MOFs exhibit high gravimetric and volumetric uptake capacities due to their high internal surfaces areas and large void volumes with some of the most impressive adsorption capacities reaching 74.2 wt% for MOF-210 at 50 bar and 298 K.[16]

The enthalpy of adsorption of carbon dioxide is a critical parameter that measures the affinity of the pore surface of the MOF toward carbon dioxide. This ultimately affects the adsorptive selectivity and the energy required to release the CO_2 molecules in the regeneration process. In order to have an effective and energy efficient MOF, this value must be carefully tuned. If the enthalpy of adsorption is too high, the energy requirement to break the CO_2 interaction with the framework and to regenerate the material becomes difficult and costly. On the other hand, if the enthalpy of adsorption value is too low, the selectivity for CO_2 decreases. The enthalpy of adsorption in MOFs, often expressed as the isosteric heat of adsorption (Q_{st}), is calculated using two or more CO_2 adsorption isotherms collected at similar temperatures (within 10 K of each other). By fitting the isotherms to a higher order polynomial equation, the Clausius-Clapeyron equation can then be used to determine the Q_{st} value.[16]

The ability for MOFs to selectively capture carbon dioxide is crucial for industrial applications of the material. Selectivity in MOFs is engineered via two mechanisms: kinetic based separation and thermodynamic based separation. In kinetic based separation, the size of the pores in the MOF plays a large role in the selective uptake of specific gases. The efficacy of this mechanism however is limited by the kinetic diameters of the gas molecules of interest. For example, the

similar kinetic diameter of CO_2 (3.30 Å) and N_2 (3.64 Å) makes it difficult for a MOF to selectively uptake CO_2 based on kinetics alone. The thermodynamic factor is driven by the difference in affinity of the various components of the gas mixture with the pore surface of the framework and can be separated into two different adsorption categories: physisorption and chemisorption. Physisorption relies on the gas molecules having different physical properties such as polarizability or the quadrupole moment, which can result in a higher enthalpy of adsorption. Returning to the example of CO_2 and N_2, CO_2 has a higher polarizability (CO_2, 29.1×10^{-25} cm^{-3}; N_2, 17.4×10^{-25} cm^{-3}) and quadrupole moment (CO_2, 13.4×10^{-40} $C \cdot m^3$; N_2, 4.7×10^{-40} $C \cdot m^3$) than N_2. These properties can be used to enhance the surface adsorption on the framework by introducing polar organic linkers or exposed metal cation sites into the framework. Chemisorption is the result of chemical interactions between certain components of the gas mixture and surface functionalities found on the MOF. A commonly used functionality in the separation of CO_2 and N_2 is amines. Due to the susceptibility of the carbon atom in CO_2 to attack by nucleophiles, the use of amines has been shown to greatly improve both the uptake capacity and selectivity for CO_2 in MOFs.

Adsorption selectivity has been calculated in two different ways. The first method uses experimental single-component gas adsorption isotherms. By using the molar ratio of the adsorption quantities at different partial pressures of the gases, a selectivity factor can be determined based on the following equation:

$$S = \frac{q_1/q_2}{p_1/p_2} \qquad (1)$$

where S is the selectivity factor, q_i represents the quantity adsorbed of component i, and p_i represents the partial pressure of component i.[16] It should be noted that this particular method does not factor in the competition of gas molecules for the adsorption sites on the pore surface. The second method used is the Ideal Adsorbed Solution Theory (IAST), which uses isotherms collected at the same temperature. In this method the single-component isotherms are first fit using equation 2:

$$\int_0^{P\cdot y_i/x_i} \frac{\text{Isotherm fit for component } i(P)}{P}\,dp = \int_0^{P\cdot y_j/x_j} \frac{\text{Isotherm fit for component } j(P)}{P}\,dp \qquad (2)$$

where x_i and y_i are the adsorbed and bulk phase mole fractions of component i, and P is the total pressure. By fitting the isotherms to this equation the mole fraction of each species in the adsorbed phase can be calculated and a projected selectivity of a mixture of two gases may be obtained. This method assumes that the two gases mix and behave as ideal gases and that the surface of the sorbent material is homogeneous.[16]

I.2.1.2 Hydrogen Storage

In an additional effort to reduce carbon emissions, alternate energy sources such as hydrogen are currently being investigated. One of the biggest obstacles in this field of research is a safe, efficient and cost effective method to store hydrogen. MOFs have demonstrated great potential in this area with the current highest uptake capacity reported by Zhou's PCN-12 (3.05 wt% at 1 bar and 77 K). [17] Despite the

high uptake value of Zhou's MOF, it still falls short of the current target set by the U.S. Department of Energy for hydrogen storage, which is 5.5% and 45 g/L at -40 ~ 60 ℃ under a maximum delivery pressure of 100 atm. [18] Therefore there is still considerable room for improvement in the field of MOFs and hydrogen storage. The two primary ways to increase the hydrogen storage capacity of MOFs is to increase the surface area/pore volume and the isosteric heat of hydrogen adsorption.

There are many ways the surface area and pore volume of a MOF can be increased. One of the most straightforward strategies is the elongation of the incorporated organic precursor ligand. By using a long alkyl chain, the surface area of the MOF has been seen to increase. Suh and coworkers have reported two different frameworks **SNU-1** and **SNU-77** which were constructed from $[Zn_4O(COO)_6]$ octahedral SBUs and tricarboxylates, NTB (**SNU-1**) and TCPBA (**SNU-77**). TCPBA is a tris(4'-carboxybiphenyl)amine that is an extended form of NTB. The result of using the elongated ligand was a much greater surface area (4180 m^2g^{-1} for **SNU-77**; 1121m^2g^{-1} for **SNU-1**).[19, 20] Although this method can be effective, the use of longer ligands has also been observed to result in the collapse of the framework after guest removal and interpenetration of the structure, which can lead to a reduced surface area or even a nonporous structure.[18] Another approach uses a mixed ligand system within the same framework which has been seen to create a highly porous structure. In the case of **SNU-6**, BPnDC and 4,4'-bpy was combined with Cu(II) to create a highly porous framework with a 83.7% solvent accessible volume and a surface area of 2590 m^2g^{-1} (Figure 7).[21]

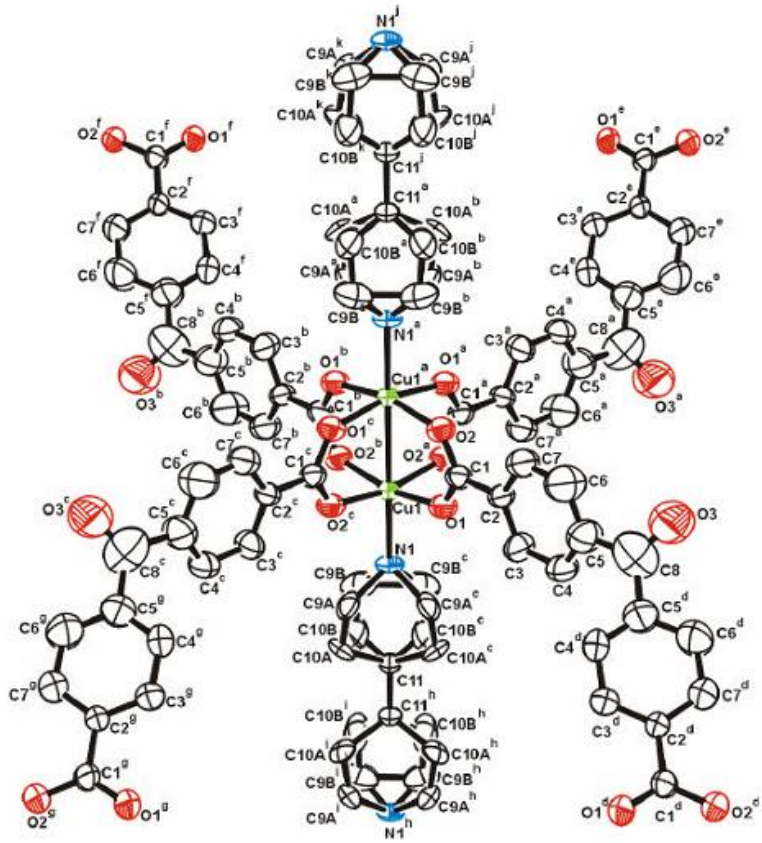

Figure 7. An ORTEP drawing of **SNU-6** showing the mixed BPnDC and 4,4'-bpy ligand system. [21]

Enhancement of the isosteric heat of hydrogen adsorption has been primarily achieved via the generation of active metal sites. By incorporating unsaturated metal centers, the Q_{st} of hydrogen adsorption has been seen to increase due to the direct interaction of H_2 molecules with these sites. Various methods for introducing these active metal sites, or "open metal sites" have been used, which include the use of metal building blocks containing open metal sites (porphyrins, salens, etc.), the attachment of organometallic complexes to the aromatic components of the struts, and the intercalation of metal complexes or solvated metal cations in the anionic frameworks.[18]

I.2.2. Heterogeneous Catalysis

MOFs are also promising candidates for heterogeneous catalysis due to the ability of the framework structures to stabilize otherwise short lived catalysts, encapsulation of molecular catalysts, coupling of catalysis to chemical separation, post-synthetic incorporation of catalytic metal sites, and substrate-size-selective catalysis.[22] One of the first reports of MOF-based catalysis was described by Fujita and co-workers on the cyanosilylation of aldehydes by a 2D MOF ($Cd(4,4'\text{-}bpy)_2(NO_3)_2$) as seen in Figure 8.[23] This particular investigation employed the substrate-size-selective route of catalysis, where the aldehydes must enter the pore channels in order to reach the active catalytic sites of the Cd(II) ions.

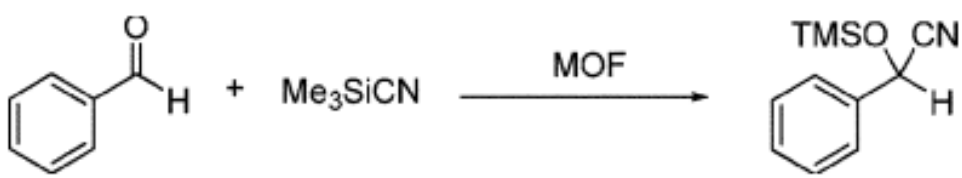

Figure 8. The scheme of cyanosilylation of an aldehyde using a MOF reported by the Fujita and coworkers.[23]

Since this report, there have been many studies that have reported the successful catalysis of reactions including: CO oxidation, oxidation of olefins, Knoevenagel condensation, alkylation of aldehydes and epoxidation of olefins to name a few.[22] One particular study involving the oxidation of CO to CO_2 was accomplished using a 3D functional MOF (**2**) constructed from a cubic SBU, $[Ni_8L_{12}]^{20-}$ (H_3L = 4,5-imidazoledicarboxylic acid), which was bridged by alkali-

metal ions (Na^+). The rate of CO oxidation, R_{QMS}, obtained by quadrupole mass spectroscopy (QMS) can be seen in Figure 9. [24]

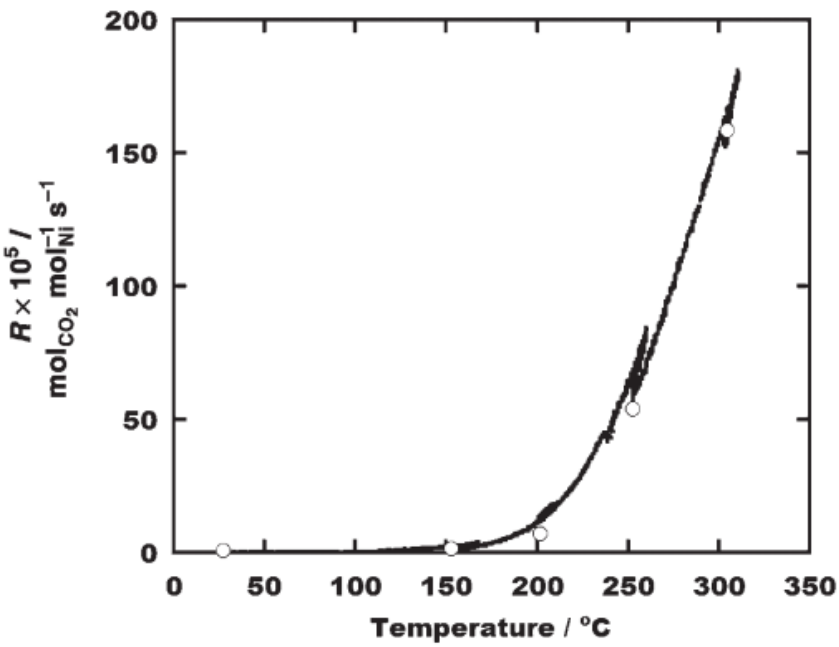

Figure 9. The rate of CO oxidation over **2** versus temperature. The R_{QMS} (line) calculated from the QMS data and R_{GC} (circles) calculated from the GC data.

Another report regarding the Knoevenagel condensation was accomplished using coordinatively unsatuated (open metal site) metal sites in chromium(III) terephthalate **MIL-101**. In this particularly study, the open metal sites on chromium provided an intrinsic chelating property with electron-rich functional groups that in turn allowed the formation of thermally stable amine species grafted on the surface. [25] The grafted amine species (ethylenediamine and diethylenetriamine) was shown to exhibit remarkably high activities in the Knoevenagel condensation reaction. It was further demonstrated that the palladium loaded **APS-MIL-101** and **ED-MIL-101** have high activities during the Heck

reaction, a method used to couple alkenes with organic moeities.

One of the most novel catalytic reactions using a composite MOF material was reported by Lin and coworkers in 2012 regarding the photocatalytic splitting of water. By synthesizing a UiO iridium functionalized photoactive framework, the Lin Group was able to reduce K_2PtCl_4 into Pt nanoparticles (2-6 nm in size) using the photoexcited iridium moiety and TEA as sacrificial electron donor. After creating this composite material, hydrogen evolution from water was observed when irradiated with visible light (Figure 10).[26]

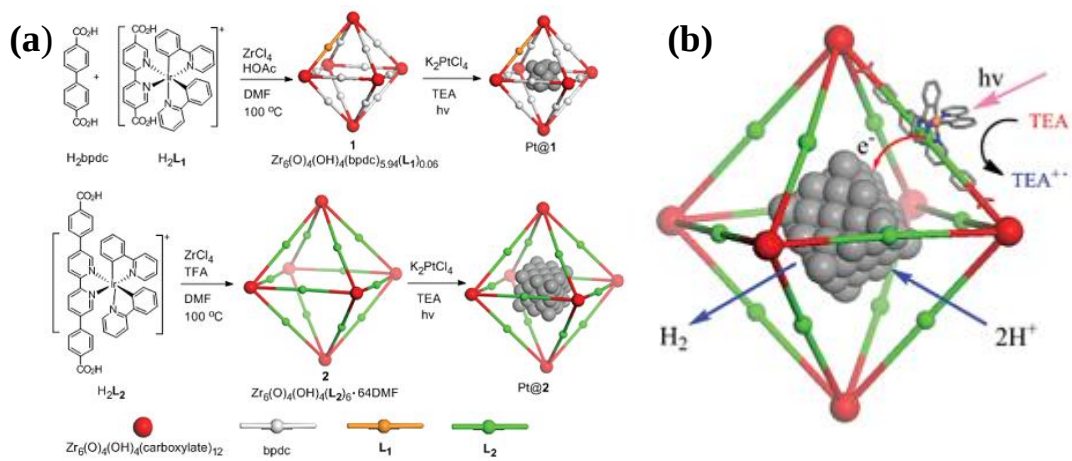

Figure 10. (a) A schematic view of the two different light sensitizing MOFs synthesized by the Lin Group used to synthesize platinum nanoparticles. (b) A scheme showing the synergistic photocatalytic hydrogen evolution process via photoinjection of electrons from the light sensitizing moiety into the Pt NPs.[26]

I.2.3. Nanoparticles and Metal Organic Frameworks

The large cavities and rigid structures of MOFs have also been proven to be suitable hosts for metal nanoparticles. The nanoparticles also impart an additional functionality to the MOF, which has been seen to result in improved heterogeneous catalysis, gas storage and chemical sensing.[18, 27-29] In particular, MOFs doped with Pd and Mg metal NPs have shown to improve hydrogen storage properties, while PCPs doped with Au and Pd have shown to catalyze alcohol, aldehyde, and CO oxidation processes.[30-32] There have been several approaches for the preparation of metal nanoparticles in the pores or supported on the surface of MOFs. These include a chemical vapor deposition method, a grinding method, and a solution impregnation method.[27, 33-37]

I.2.3.1 Chemical Vapor Deposition Method

One of the first reported methods to fabricate metal nanoparticles within MOF structures employed a solvent-free gas-phase loading technique. By using a volatile metal organic compound, the metal nanoparticle precursor can be incorporated into the channels or pores of the MOF, avoiding the potential problem of stability in certain solvents. After "loading" the metal organic compound within the framework, the precursor is reduced, thus creating nanoparticles within the pores and channels of the MOF. An advantage of this particular method is the high loading levels of up to 30-40 wt.-% in a single step. One of the earliest reports of this nanoparticle loading method was reported by the Fischer Group in 2005.[34] In this paper, Cu, Au, and Pd nanoparticles were loaded inside **MOF-5** using the following precursors: $[(\eta^5\text{-}C_5H_5)Cu(PMe_3)]$, $[(CH_3)\text{-}Au(PMe_3)]$ and $[(\eta^5\text{-}C_5H_5)Pd(\eta^3\text{-}C_3H_5)]$. The

obtained composite material was characterized using IR spectroscopy, inductively coupled plasma atomic emission spectroscopy (ICP-AES), PXRD, solid state NMR spectroscopy and transmission electron microscopy. Since Fischer's report, there have been multiple papers that have used the same chemical vapor deposition method to create Ru, Pt, and Mg nanoparticles within host framework structures.

I.2.3.2 Solid Grinding Method

The deposition of metal nanoparticles into MOFs has also been achieved by solid grinding of a volatile precursor together with an activated MOF material.[38] During grinding, the volatile precursor is sublimated and diffuses into the cavities of the MOF. Although this method is essentially a modified chemical vapor deposition method, this particular synthetic route results in a better distribution of the precursor within the host structure. This method was used to synthesize nanosized gold clusters within MOF-5, $[Cu_3(btc)_2]$, [Al(OH)(bdc)], ZIF-8, CPL-1 and CPL-2.[38] The resulting nanoclusters were found to be monodisperse with particle sizes below 2 nm (Figure 11).

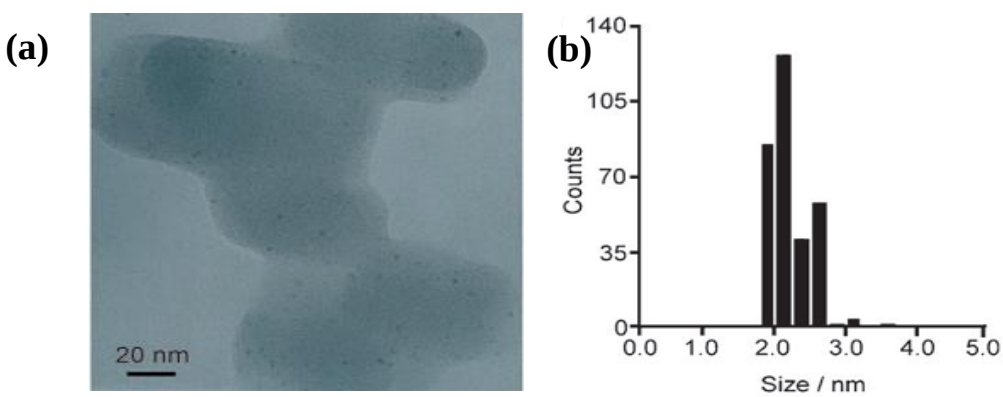

Figure 11. Au nanoclusters formed inside CPL-2 using the solid grinding method. (a) TEM image of the loaded nanoparticles. (b) Histogram of the nanoparticles.[38]

I.2.3.3 Solution Impregnation Method.

Another well studied technique in the fabrication of metal nanoparticles is the solution impregnation technique. As the name implies, the host MOF is loaded with the metal precursor in a liquid phase as opposed to the vapor phase used by the chemical vapor deposition and solid grinding method. The metal salt is then reduced by an external chemical reducing agent such as hydrazine.[39] Another reduction pathway can occur from the framework itself (autoreduction). This technique was first reported by Suh and coworkers in 2005, where the Ni(II) building block was oxidized to Ni(III), creating silver nanoparticles.[40] Since this study, there have been several reports of nanoparticles synthesized by the similar solution impregnation technique using redox-active MOFs.[31-33, 41] In one particularly interesting redox-active framework, Pd nanoparticles were formed by a redox reaction between the organic linker $\{[Zn_3(ntb)(EtOH)_2]\cdot 4EtOH\}_n$ where ntb = 4,4' ,4'' –nitrilotrisbenzoate, and the palladium salt $Pd(NO_3)_2\cdot 2H_2O$ as shown in Figure 12.[32] One distinct advantage of the solution impregnation technique using

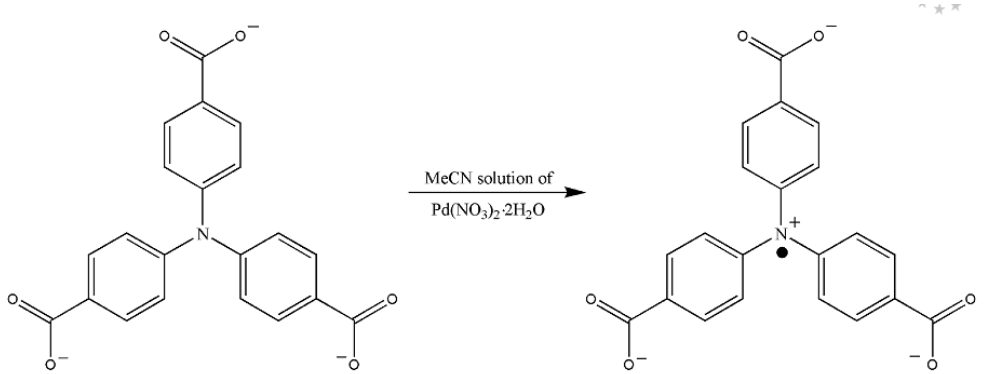

Figure 12. A schematic representation of the redox reaction of the ntb linker with $Pd(NO_3)_2$ salt.[32]

a redox active framework is that the amount of NPs formed can be controlled by the immersion time and a stoichiometric amount of NPs can be generated within the cavities of the framework while maintaining the original framework structure. Additionally, the use of a redox active framework removes the need of any additional reducing agent or capping agent.

I.2.3.5 Structural Characterization

One of the most challenging obstacles in nanoparticle loaded MOF composite structures is characterization. In order to accurately and precisely determine the location of the fabricated nanoparticles multiple techniques must be used. Nanoparticles have been found to be localized on the surface of the host (Figure 13A), distributed throughout the volume of the host with large size distributions (Figure 13B) and distributed throughout the host exhibiting an average particle size matching the pore dimensions (Figure 13C). Transmission electron microscopy (TEM) is one of the most valuable techniques to obtain accurate information about the location of the nanoparticles within the host.

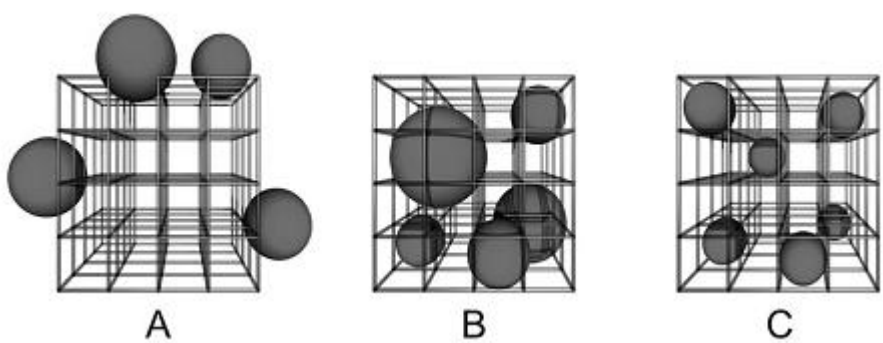

Figure 13. The three different possible locations and distributions of metal nanoparticles within the host MOFs.[27]

Different TEM techniques such as bright field TEM (BF-TEM), high angle annular dark field scanning TEM (HAADF-STEM) and tomography reveal important information regarding the composite material. One particular drawback of this technique is the 2D nature of the obtained image. It is therefore necessary to perform a tomographic measurement in order to obtain the exact three-dimensional structural environment.[27]

One problem that arises from characterization of these materials is the appearance of artifacts during the characterization process itself. During TEM imaging, the sample is exposed to a strong electron beam, which has been shown to degrade or collapse the whole framework. Therefore imaging of the sample must be done with great care. For example, exposure of [Cu_3btc_2] to a strong electron beam results in the formation of Cu and Cu_xO particles.[27] Agglomeration of the as-synthesized particles has also been shown to take place during imaging.[37]

Other characterization techniques needed in order to properly characterize the resulting composite MOF nanoparticle material include as PXRD, UV/Vis spectroscopy, and energy dispersive x-ray spectroscopy (EDS) or x-ray photoelectron spectroscopy (XPS). PXRD allows reveals the effect of the formation of nanoparticles on the host framework structure. In some cases the formation of the respective nanoparticles has been seen to change the original structure of the host as evidenced by the PXRD pattern. Additionally, the PXRD pattern may reveal peaks arising from the nanoparticles, which generally appear at higher 2θ angles (e.g. 38° for Au (111)). The use of UV/Vis spectroscopy can also help to elucidate the true location of the particles within the host due to the surface

plasmon resonance effect arising from the nanoparticles. EDS and XPS is primarily used to determine the elemental composition of present elements and can confirm whether the nanoparticle of interest was synthesized.

I.3. Metal Nanoparticles

Nano-sized metallic particles with well-defined size have garnered great attention due to the potential applications in magnetism, optics, electronics, separation, clinical diagnostics, sensors, therapeutics, drug delivery, and catalysis.[42-46] Due to the quantum effect, metal nanoparticles exhibit unique properties that are inherently different from the bulk sample. One of the challenges in this field of research is the precise control of size and morphology and many studies have been performed to determine the most efficient and effective method to create the desired shape and size of the metal of interest. Various methods have been used such as chemical reduction,[47] thermal decomposition,[48] microwave-assisted reduction,[49] photochemical reduction,[50] sonochemical deposition[51] and electrochemical reduction.[52] One of the most useful methods in nanoparticle preparation is template synthesis, in which uniform void spaces of porous materials may be used to confine and control the growth of the nanoparticles as a guest.

I.3.1 Gold Nanoparticles

The synthesis and morphological control of gold NPs have attracted great interest due to their shape dependent properties.[53] The shapes of the gold NPs affect the optical, physical, and catalytic properties.[54, 55] Some examples of methods used to control the specific shapes of gold nanoparticles include a seed mediated and a UV-

assisted approach.[56, 57]

The seed mediated method of synthesizing shaped gold nanoparticles is the most frequently used, and commonly involves a two-step process. The first step involves the nucleation/generation of reasonably uniform, spherical seed particles from a supersaturated solution of gold ions. In the second step, the reaction conditions are altered to more mild conditions, where more gold ions are added together with some type of shape templating surfactant or molecule that directs the growth of the gold nanoparticle into a specific desired shape.[53] Depending on the shape directing agent, gold nanorods, triangles, cubes, or hexagons may be synthesized. In one particular study, the effect of two different halide ions (Cl^- and Br^-) was investigated to show that when used in accordance with silver ions, two different morphologies could be obtained. In the seed mediated growth process, the use of chloride ions was seen to result in concave cubes, while the use of bromide ions was seen to result tetrahexahedra explained by a binding of the halide to the surfactant molecule, cetyltrimethylammonium (CTA) to form CTA-X (X = Cl^-, Br^-) as seen in Figure 14.[58]

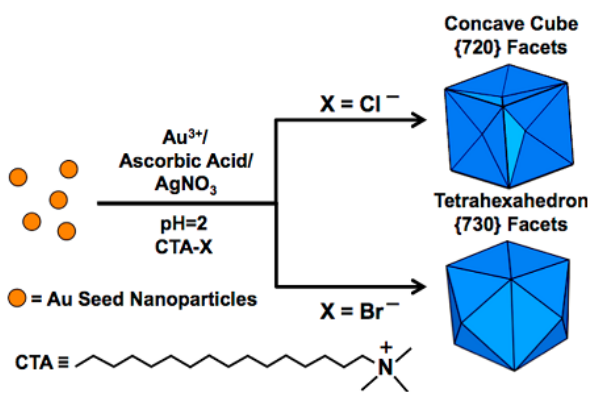

Figure 14. The effect of two different halide ions in a seed-mediated growth process of gold nanoparticles in the presence of a silver ion additive and CTA.[58]

The UV-assisted approach has been demonstrated to result in plate-like triangular gold nanoparticles. In a study done by Chen and coworkers, $HAuCl_4$ was used as a precursor in addition with polyvinyl alcohol (PVA) as the capping agent. When the growth solution was irradiated with a low-pressure mercury lamp (λ = 253.7 nm) for 48 hours at 15℃, the triangular shaped nanoparticles were seen to form (Figure 15). Although the explicit effect of UV irradiation was not explained in the study, the Kossel-Stranski theory of face selective growth of crystals was used to support the resulting triangular shaped nanoparticles. [59]

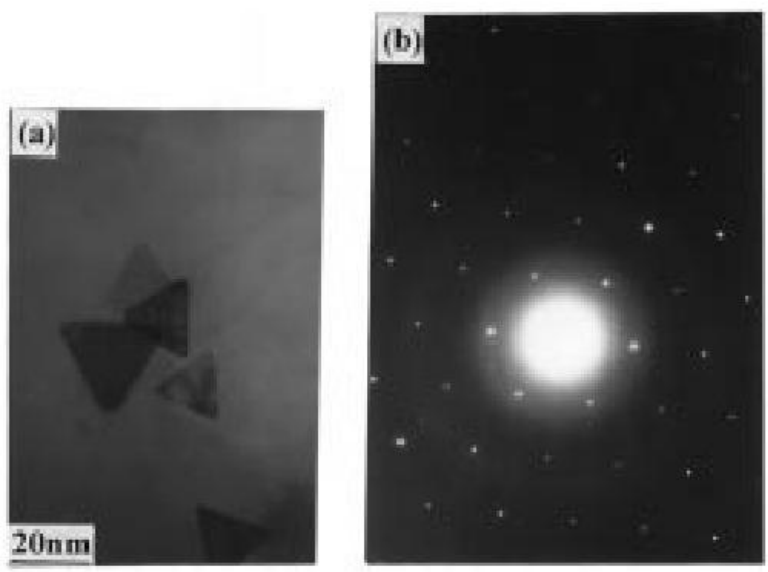

Figure 15. (a) The resulting triangular shaped gold nanoparticles upon UV irradiation of a gold nanoparticle growth solution. (b) The corresponding electron diffraction pattern for the triangular gold nanoparticles.

As mentioned previously, MOFs have been shown to be capable of synthesizing gold nanoparticles via the chemical vapor deposition method as reported by Fischer and coworkers in 2005.[34] The synthesis of gold nanoparticles

using redox active MOF was first reported in 2006 by Suh and cowoerkers.[41] However, there has yet been no report of shaped gold nanoparticles synthesized using a MOF.

I.3.2 Platinum Nanoparticles

Platinum nanoparticles have also drawn increasing interest due to their applications in catalytic processes.[60] One of the most alluring catalytic reactions involving hydrogen is the reduction of water to form H_2 gas. In these systems platinum is used as a catalytic active site as seen in Scheme 1.[61]

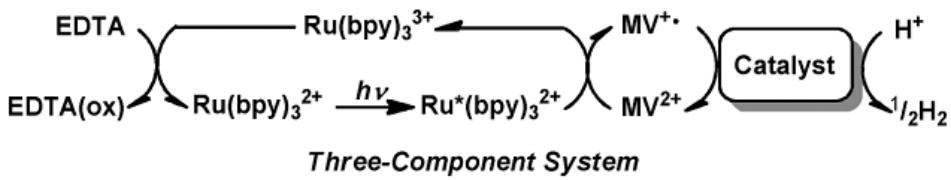

Scheme 1. A three-component-system driving photochemical H_2 production from water.

In this particular system EDTA is used as a sacrificial electron donor, while $Ru(bpy)_3^{2+}$ is used as a light sensitizing unit. The methyl viologen (MV) acts as an electron relay to the catalyst which then splits water into hydrogen and oxygen gas.

Various preparation methods for platinum nanoparticles have been reported including chemical reduction, surfactant mediated growth, sonochemical and microwave assisted synthesis, and chemical vapor deposition.[29, 62-64] The most common route of platinum nanoparticle synthesis uses an aqueous hexachloroplatinate which is consequently reduced using hydrogen gas or $NaBH_4$. Recently, the Lin group reported that Pt nanoparticles were fabricated in MOFs by

the photoreduction of K_2PtCl_4 in the presence of TEA that acted as a reductive quencher and electron donating species.[26] Amongst all of these processes, however, there has not been a MOF that is capable of producing Pt nanoparticles without the assistance of an external mediator.

II. Experimental Section

General Method. $[Ni_2(C_{26}H_{52}N_{10})Cl_4]\cdot H_2O$, H_2bpydc and $Ru(DMSO)_4Cl_2$ were prepared according to the reported procedures.[65-67] All other chemicals and solvents used in the synthesis were of reagent grade and used without further purification. UV/Vis spectra were recorded with a PerkinElmer Lambda 35 UV/Vis spectrometer. Infrared spectra were recorded on a Perkin Elmer Spectrum One FT-IR spectrophotometer. NMR spectra were measured on a Bruker Spectrospin 300 spectrometer. Elemental analyses were performed with a PerkinElmer 2400 Series II CHN Analyzer. Thermogravimetric analyses (TGA) and differential scanning calorimetry (DSC) were performed under N_2 (g) at a scan rate of 5 °C min^{-1}, using a TGA Q50 and a DSC Q10 of TA Instruments, respectively. Powder X-ray diffraction data were recorded on a Bruker New D8 Advance diffractometer at 40 kV and 40 mA for Cu Kα (λ = 1.54050 Å), with a scan speed of 0.5s per step and a step size of 0.02° in 2 θ. High Resolution TEM (HRTEM) images, energy-dispersive X-ray spectra (EDS), and high angle annular dark field scanning TEM (HAADF-STEM) images were obtained with JEM-3000F (JEOL) and Tecnai F20 (FEI) that were equipped with an Oxford INCA EDS unit. Electron paramagnetic spectra (EPR) were obtained with a JES-TE200 (JEOL).

Preparation of Na_2(bpydc): 2,2'-bipyridine-5,5'-dicarboxylic acid(H_2bpydc) (1.00 g, 4.10 mmol) was dissolved in water(10.00 mL) in the presence of an excess amount of NaOH (0.500 g, 12.50 mmol). The solution was reduced to the minimum volume, and methanol was added to precipitate out the product. The product was filtered, washed with methanol, and dried. Elemental analysis Found: C, 49.05; H, 2.08; N, 9.61. Calc. for $Na_2C_{12}H_6N_2O_4$: C, 50.02; H, 2.10; N, 9.72%.

Preparation of $[Ni_2(C_{26}H_{52}N_{10})Cl_4]\cdot H_2O$: $NiCl_2 \cdot 6H_2O$ (4.75 g, 20 mmol) was dissolved in methanol (120 mL). *N,N'*-Bis(2-aminoethyl)diaminopropane (3.30 mL, 20 mmol) was slowly added to the solution and the solution turned violet. *p*-Xylylenediamine (1.36 g, 10 mmol) and an excess amount of paraformaldehyde (2.40 g, 80 mmol) were added to the solution, then the mixture was refluxed for 5 days until the colour of the mixture turned to dark brown. The mixture was cooled down to room temperature and pink precipitate formed. The mixture was then filtered and washed with MeOH thoroughly. The filtered product was dried in vacuo and recrystallized in water/methanol. Elemental analysis Found: C, 39.93; H, 6.48; N, 17.79; Calc for $Ni_2C_{26}H_{54}N_{10}Cl_4O$: C, 39.94; H, 6.96; N,17.91.

Preparation of $Ru(DMSO)_4Cl_2$: $RuCl_3 \cdot 3H_2O$ (1.00 g, 3.8 mmol) was dissolved in DMSO (5 mL). The solution was then refluxed for 5 minutes. After reducing the volume to half in vacuo, the addition of acetone (20 mL) induced a bright yellow precipitate. The complex was filtered and washed with acetone thoroughly and dried in vacuo. Elemental analysis Found: C, 19.88; H, 4.94; N, 0.00; Calc for $RuCl_2C_8H_{24}O_4S_4$: C, 19.85; H, 5.00; N,0.00.

Preparation of $\{[Rubpydc_3Ni_2(C_{26}H_{52}N_{10})]\cdot 14H_2O\}_n$ (SNU-M55). An aqueous solution (2 mL) of $Ru(DMSO)_4Cl_2$ (24.2 mg, 0.05 mmol) was carefully layered over an aqueous solution of Na_2(bpydc) (43.2 mg, 0.15 mmol) (2 mL) in a test tube (Scheme 2). To this layered solution, an aqueous solution (6 mL) of $[Ni_2(C_{26}H_{52}N_{10})Cl_4]\cdot H_2O$ (39.1 mg, 0.05 mmol) was added to form a three-layered solution. The reaction vessel was sealed and allowed to stand at room temperature for 2 weeks. A dark brown crystalline product was formed, which was filtered and

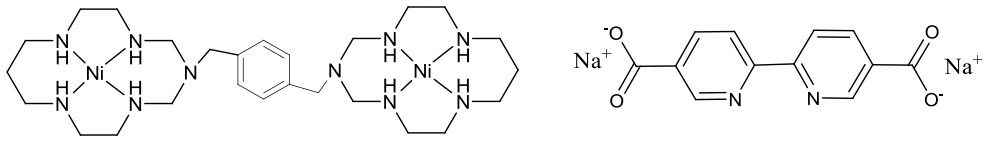

+

$RuCl_2(DMSO)_4$

SNU-M55

Scheme 2. The three molecular building blocks combined to create SNU-M55.

washed briefly with water. Yield: 57 mg (55%). Elemental analysis found: C, 42.82; H, 5.83; N, 12.55; Calc. for $C_{62}H_{98}N_{16}O_{26}RuNi_2$: C, 42.90; H, 5.69; N, 12.91%. FT-IR (KBr, cm^{-1}): 3400 (s, br.-OH), 3192 (m, br. -NH), 2923 (w), 2863 (w), 1612 (s, $-COO^-$), 1371 (s), 1039 (w), 992 (w), 838 (m), 779 (m), 703 (m). UV/Vis λ_{max} (diffuse reflectance)/nm 495, 419 sh.

Preparation of [Ni(cyclam)(bpydc)]·5H$_2$O. [Ni(cyclam)]$(ClO_4)_2$ (0.314 g, 0.69 mmol) was dissolved in hot water (7 mL), and a hot aqueous solution (2 mL) of Na_2bpydc (0.199 g, 0.69 mmol) was added dropwise. The yellow solution was

allowed to stand at room temperature until pale yellow crystals formed, which were filtered off, washed with water, and dried in air. Yield: 0.273 g, 67%. Elemental analysis found: C, 44.42; H, 6.87; N, 14.17; Calc. for $NiC_{22}H_{40}N_6O_9$: C 44.68, H 6.82, N 14.21; found: C 44.83,H 6.81, N 14.24.

Preparation of Au and Pt nanocomposite: In each case, the framework (20.3 mg, 0.01 mmol) was immersed in an aqueous solution (5 mL, 34 mM) of $NaAuCl_4$•$6H_2O$ and K_2PtCl_4 respectively, for 10 minutes. The heterogeneous solution was then filtered and washed 5 times with water to remove any excess metal salt.

UV/Vis spectra were measured for the filtrate resulting from the immersion of **SNU-M55** in the K_2PtCl_4 solution.

Comparative Study using Molecular building blocks: In each case, the molecular building blocks: Na_2bpydc, $[Ni_2(C_{26}H_{52}N_{10})Cl_4]\cdot H_2O$, and $RuCl_2(DMSO)_4$ (0.01 mmol) was immersed in an (5 mL, 34 mM) of $NaAuCl_4\bullet 6H_2O$ and K_2PtCl_4, respectively, for 10 minutes. The heterogeneous solution was then filtered and washed 5 times with water to remove any excess metal salt.

Comparative Study using [Ni(cyclam)(bpydc)]·5H_2O: In each case, the framework (0.01 mmol) was immersed in an aqueous solution (5 mL, 34 mM) of $NaAuCl_4\bullet 6H_2O$ and K_2PtCl_4, respectively, for 10 minutes. The heterogeneous solution was then filtered and washed 5 times with water to remove any excess metal salt.

Hydrogen Evolution Measurements: Hydrogen evolution measurements were carried out using a 100 W tungsten-halogen lamp (Osram, model 64637). The sample cell was custom built based on the design reported by Ken Sakai (Kyushu University) and can be seen in Figure 15a, 15b. The sample cell was made of hollow aluminium walls and was fitted with quartz windows. The hollow walls were connected to a water circulator so that the sample containing water bath temperature could be maintained at a constant 18˚C. The sample cell itself was a 15 mL vial fitted with a gas tight Teflon lid fitted with gas tight septum which allowed extraction of the head gas using a gas tight syringe (Figure 15c). The light intensity was measured using a light flux measuring probe set (Oriel, model 70260 and 70268, window size 1.1 cm^2). Analysis of the head gas of the reaction vial was performed using an Agilent 6890N GC, equipped with a 13X Molecular Sieves

packed column (2 m length, 2.0 mm inner diameter, 1/8 inch outer diameter) and a thermal conductivity detector. High purity argon gas (99.993 %) was used as a carrier. The column temperature was set to 40℃ and the detector port was set to 80℃.

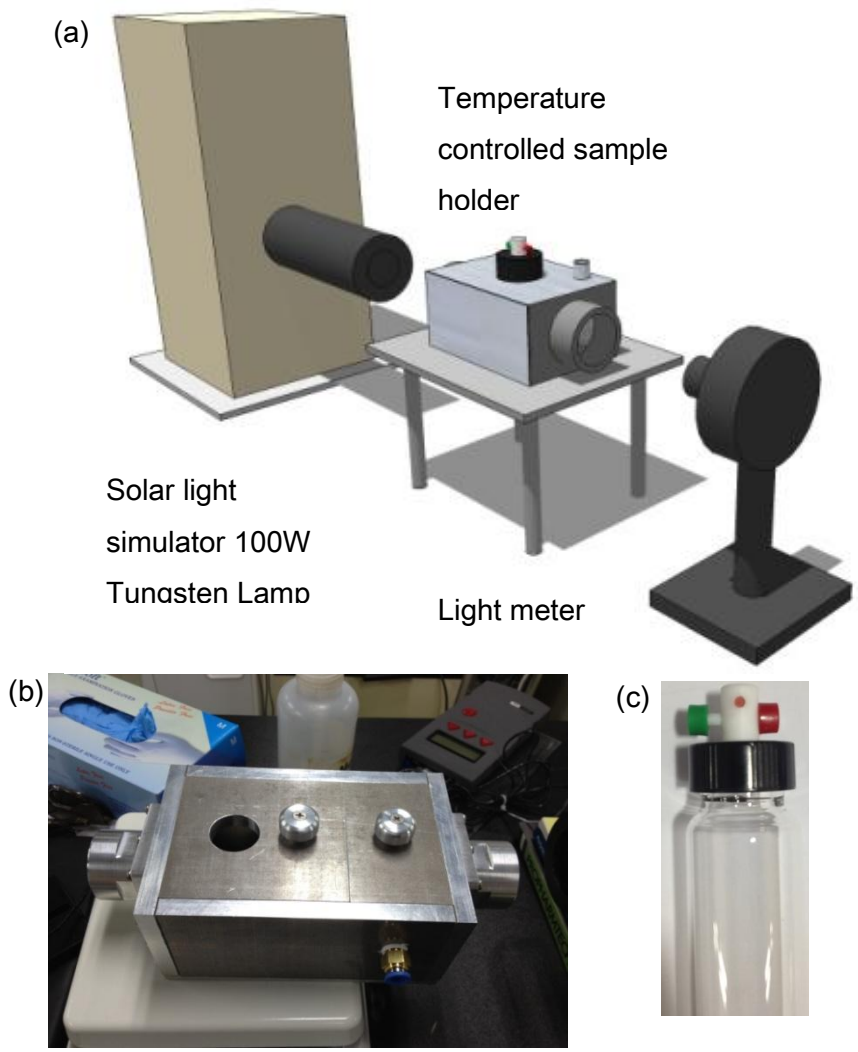

Figure 16. (a) A rendered image of the hydrogen evolution measurement apparatus showing the light source, sample holder, and light meter. (b) sample holder. (c) sample cell fitted with a gas tight Teflon lid with gas tight septum.

X-ray Crystallographic Analysis. Diffraction data of **SNU-M55** was collected on an Enraf Nonius Kappa CCD diffractometer with graphite-monochromated Mo Kα radiation (λ = 0.71073 Å). The single crystal was coated with paratone-*N* oil and the diffraction data were measured at 100K. Preliminary orientation matrixes and unit cell parameters were obtained from the peaks of the first 10 frames and then refined using the whole data set. Frames were integrated and corrected for Lorentz and polarization effects by using DENZO.[68] The scaling and global refinement of crystal parameters were performed by SCALEPACK. No absorption correction was made. The crystal structure was solved by direct methods[69] and refined by full-matrix least-squares refinement using SHELXL-97 computer program.[70] the hydrogen atoms were positioned geometrically using a riding model. The structure refinement was further performed after modification of X-ray data by ignoring the disordered guest solvent molecules. CCDC-927153 (**SNU-M55**) contains the supplementary crystallographic data for this compound. These data can be obtained free of charge from The Cambridge Crystallographic Data Centre via www.ccdc.cam.ac.uk/data_request/cif.

III. Results and Discussion

III.1. X-ray structure and properties of {[Rubpydc$_3$Ni$_2$($C_{26}H_{52}N_{10}$)] ·14H_2O}$_n$ (SNU-M55).

SNU-M55 was synthesized by the self assembly of Ru(DMSO)$_4Cl_2$, Na_2(bpydc) (bpydc = 2,2'-bipyridine-5,5'-dicarboxylate), and [$Ni_2(C_{26}H_{52}N_{10})Cl_4$]·$H_2O$ in aqueous solution. The resulting large dark brown crystals showed excellent crystallinity and was insoluble in water. The single crystal X-ray structure of **SNU-M55** reveals that each Ru(II) center is coordinated to three bpydc^{2-} ligands through the N-pyridine donor sites, creating an octahedral coordination geometry. Two of the three bpydc^{2-} ligands coordinate four Ni(II) centers of four different bismacrocyclic complexes via the deprotonated carboxylate moieties. The remaining one bpydc^{2-} ligand coordinated to the Ru(II) center is left uncoordinated in a deprotonated form in order to maintain the charge balance of the framework. The fundamental building unit of **SNU-M55** can be seen in Figure 17.

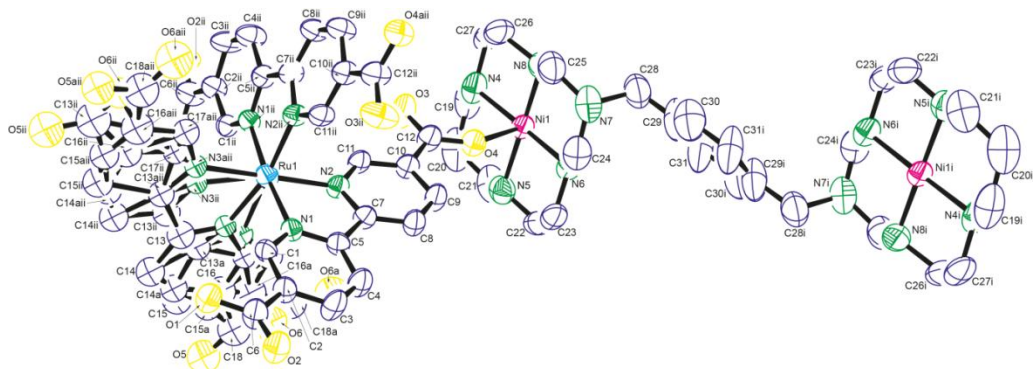

Figure 17. An ORTEP drawing of **SNU-M55**, showing the coordination environment of bismacrocyclic Ni(II) unit and $Ru(bpydc)_3^{2+}$ moiety. Due to the thermal disorder of one of the uncoordinated $bpydc^{2-}$ units, the structure was isotropically refined. The structure shows that the bpydc unit is equally disordered over two positions. Thermal ellipsoids are drawn with 30% probability. Symmetry transformations: i, -x+1, -y-1, -z+1; ii, x+1, y, -z+3/2;

Table 1. Crystallographic data for **SNU-M55.**

	SNU-M55
Formula	$Ru\ Ni_2\ C_{62}\ H_{64}\ N_{16}\ O_{12}$
Crystal system	*Monoclinic*
Space group	*C 2/c*
Formula weight	1443.73
a, Å	23.269(5)
b, Å	20.397(4)
c, Å	21.738(4)
β, °	115.59(3)
V, Å ^{3}	9305.0(4)
Z	4
ρ_{calcd}, g cm^{-3}	1.031
T, K	100(2)
λ, Å	0.71073
μ, mm^{-1}	0.612
Goodness-of-fit on F^2	1.312
F(000)	2976
Reflections collected	6452
Independent reflections	6452 [*R*(int) = 0.0996]
Completeness to θ = 25.0°	98.3%
Data / restraints / parameters	6452 / 149 / 404
θ range for data collection, °	1.94 to 26.45
Diffraction limits (*h*, *k*, *l*)	0<=h<=29, 0<=k<=25, -23<=l<=27
Refinement method	Full-matrix least-squares on F^2
R_1, wR_2 [$I > 2\sigma(I)$]	0.0996,[a] 0.3003[b]
R_1, wR_2 (all data)	0.1137,[a] 0.315[b]
Largest diff. peak and hole, e Å $^{-3}$	1.837, -0.958

[a] $R = \Sigma||F0| - |Fc||/\Sigma|F0|$. [b] $wR(F^2) = [\Sigma w(F_o^2 - F_c^2)2/\Sigma w(F_o^2)^2]^{½}$ where $w = 1/[\sigma^2(F_o^2) + (0.2000\ P)^2 + (0.0000)P]$, $P = (F_o^2 + 2F_c^2)/3$

The overall connectivity results in a 2D layer (Figure18a). These 2D layers (shown in blue in Figure 18b) are connected to each other via the xylylene moieties (shown in yellow in Figure 18b) of the bismacrocyclic complexes, which act as pillars to create a 3D network. The distance between the two Ni(II) centers of the bismacrocyclic complex is 12.42 Å, and the xylylene pillar is tilted by 62° to give a distance of 5.82 Å between the 2D layers. The framework generates one dimensional rectangular channels running along the [101] direction with the effective window size of 8.32 x 6.53 $Å^2$ (shown in Figure 18c). The void volume of **SNU-M55** is 42.7% as estimated by PLATON.[71] The guest solvent molecules included in **SNU-M55** could not be refined due to the severe thermal disorder even when the X-ray data were collected at 100 K. The solvent molecules ($14H_2O$) solvent molecules included in **SNU-M55** could not be refined due to the severe thermal disorder even when the X-ray data were collected at 100 K. The solvent molecules ($14H_2O$) were determined by the elemental analysis data and thermogravimetric analysis (TGA) (Figure 19). The TGA data for **SNU-M55** measured under a N_2 atmosphere indicated that it lost solvent guest molecules as soon as it was removed from the mother liquor. It lost 15.0% weight upon heating to approximately 100°C. The framework was shown to decompose at 285°C. The measured PXRD pattern of the as-synthesized framework is almost coincident with that of the simulated pattern derived from the X-ray single crystal raw data, showing that the bulk sample is the same as the single crystal (Figure 20).

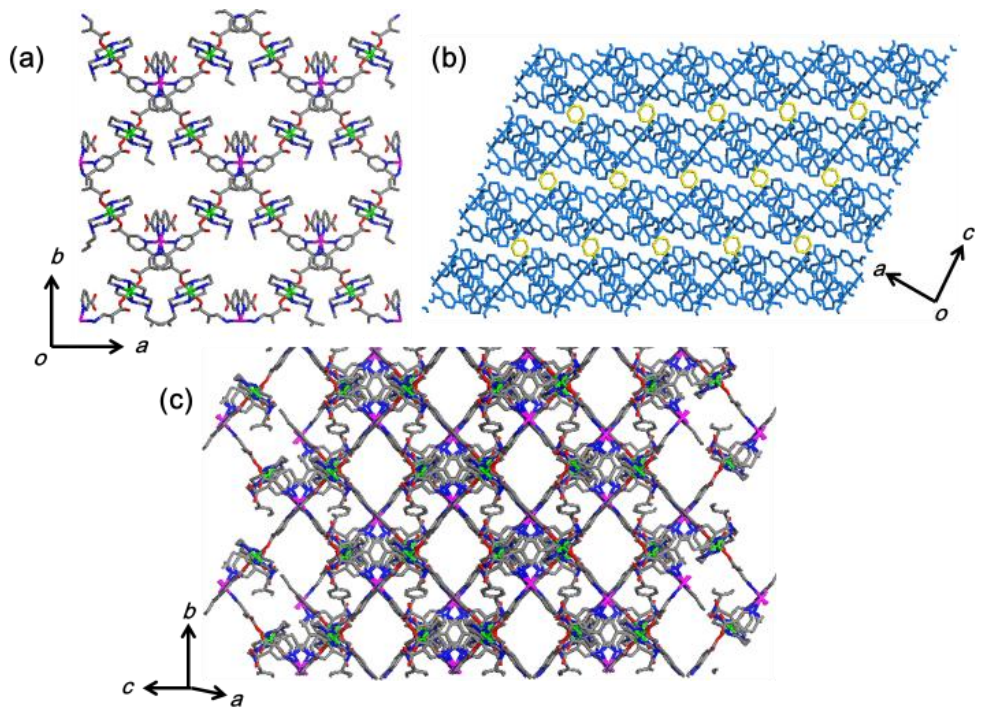

Figure 18. The X-ray structure of **SNU-M55**. (a) A view of the 2D layer in the ab plane as seen in the [001] direction (xylylene moiety in the bismacrocycle is omitted for clarity). (b) A view of the stacking arrangement of the 2D layers via the xylylene pillar. (c) A view showing the 1D channels running along the [101] direction of the framework.

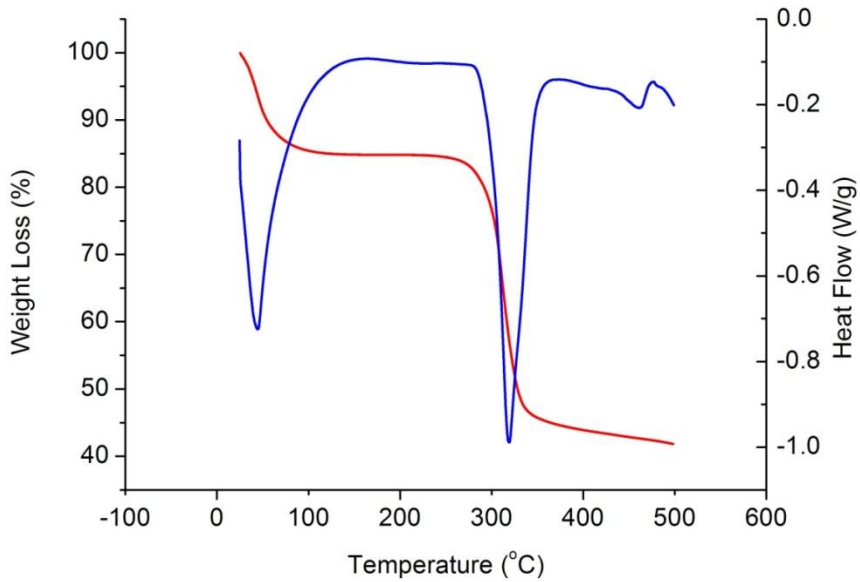

Figure 19. TGA/DSC traces for as synthesized **SNU-M55.**

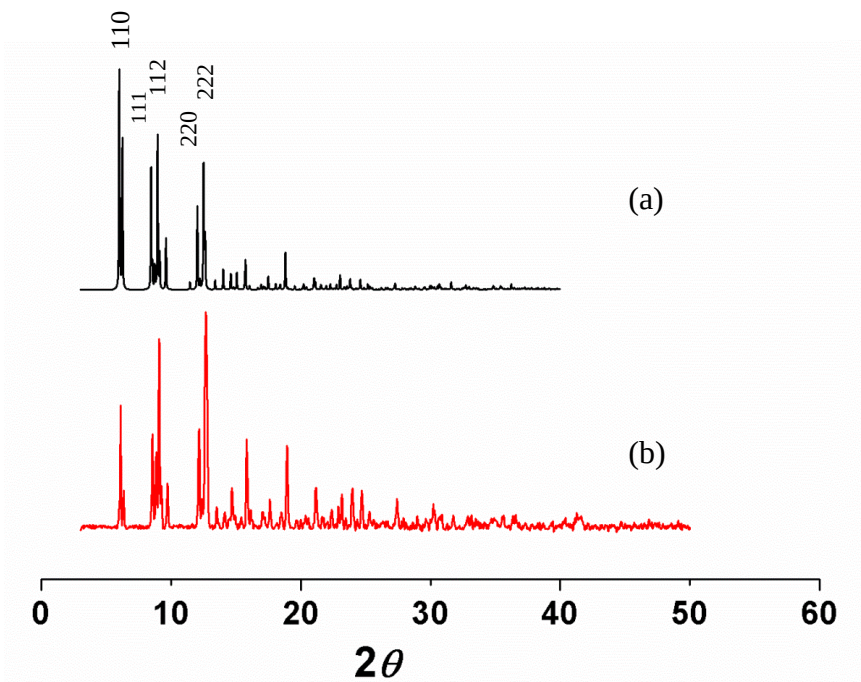

Figure 20. The simulated (a) and measured (b) PXRD patterns for **SNU-M55**.

Spectroscopic Properties

The $Ru(bpy)_3^{2+}$ moiety is well known for its dye sensitizing ability and absorbs light over the entire visible light region as observed in the diffuse reflectance spectrum (Figure 21). λ_{max} values were observed at 419 and 501 nm respectively. The particularly strong absorbance exhibited by **SNU-M55** can be explained by the relationship between the *d* orbitals of the metal and π orbitals of the ligand. Since Ru^{2+} is a d^6 metal, it has a completely filled t_{2g}^6 configuration therefore easily forms a stable complex with diimine ligands through π-back-donation.[72, 73] Metal-to-ligand charge transfer (MLCT) plays a significant role in the spectroscopic properties of those complexes. [62]

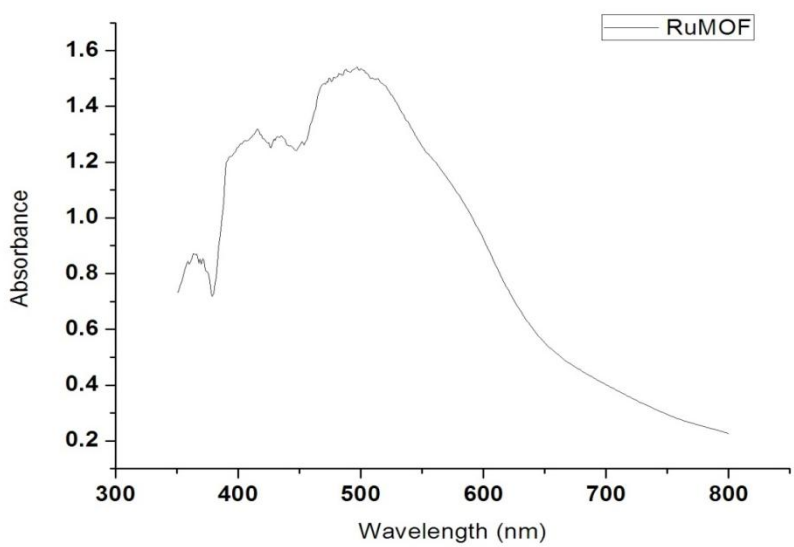

Figure 21. Diffuse reflectance spectrum of **SNU-M55.**

III.2. Formation of Au and Pt Nanoparticles Using the Redox Properties of SNU-M55

Since **SNU-M55** contains bismacrocyclic Ni(II) complexes as well as $Ru(bpydc)_3^{2+}$ moieties, both of which can be redox-active, we have tried to synthesize Au and Pt nanoparticles by the redox reaction between this framework and the corresponding metal salts. In each case, the framework (0.01 mmol) was immersed in an aqueous solution (5 mL, 34 mM) of a metal salt ($NaAuCl_4 \cdot 6H_2O$, K_2PtCl_4) for 10 minutes, which resulted in the formation of each respective metal nanoparticle. In organic solvents systems (MeCN, EtOH, and MeOH) instead of the aqueous solution, the immersion technique using **SNU-M55** in the solutions of $NaAuCl_4 \cdot 6H_2O$ and K_2PtCl_4, respectively, afforded gold nanoparticles but no platinum nanoparticles due to the insolubility of K_2PtCl_4 in these solvents. The metal nanoparticles were characterized by high resolution transmission electron microscopy (HRTEM), high-angle annular dark-field scanning transmission microscopy (HAADF-STEM), energy dispersive X-ray spectroscopy (EDS), and PXRD.

III.2.1 Gold Nanoparticles.

Gold nanoparticles of sizes ranging from 5-15 nm are formed (Figure 22) in addition to larger triangular, square, and hexagonal shaped nanoparticles ranging 20 - 75 nm in size (Figure 23), which are much bigger than the channel size of the host determined by the X-ray crystal structure. The gold nanoparticles were identified by HRTEM, showing the d-spacing value of 2.349 Å (ICDD PDF no. 00-004-0784 d = 2.355 Å Au).

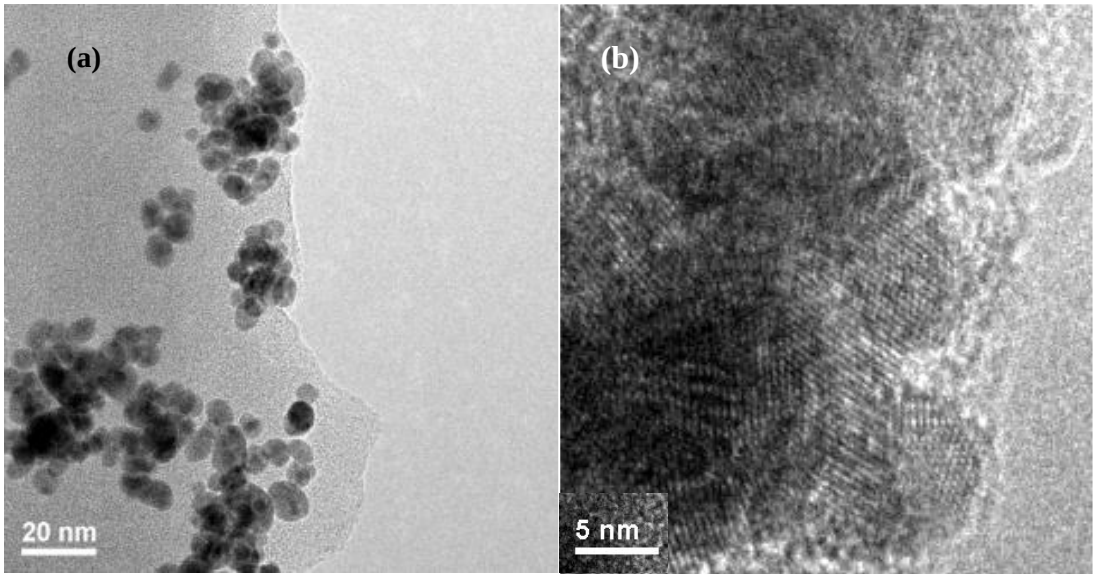

Figure 22. (a) HRTEM image of gold nanoparticles formed within **SNU-M55**. (b) A zoomed in image of the same sample showing the lattice fringes of the gold nanoparticles.

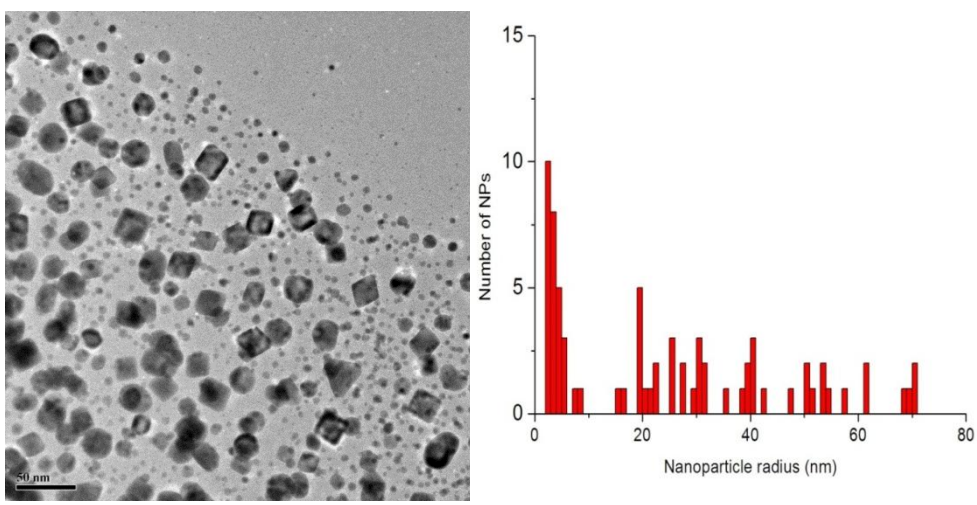

Figure 23. (a)TEM image of shaped gold nanoparticles formed within **SNU-M55**. (b) A size distribution histogram of the nanoparticles formed in **SNU-M55**.

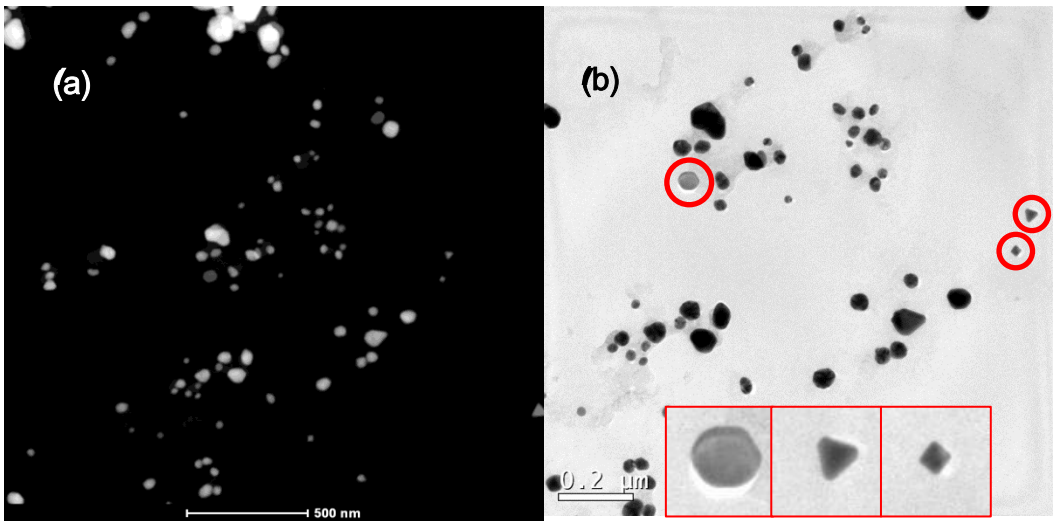

Figure 24. (a) The HAADF-STEM image of gold nanoparticles formed on the surface of **SNU-M55.** (b) The BF-TEM image of gold nanoparticles formed in **SNU-M55.**

The location of the gold nanoparticles was determined to be on the surface of the host as evidenced by HRTEM, HAADF-STEM, and BF-TEM. Closer inspection of the HRTEM image shows that the Au NPs form mainly at the edges of the host, suggesting that the nanoparticles are located on the outer surface of the MOF solid. Using HAADF-STEM and BF-TEM imaging, the inner part of the matrix can also be seen to be devoid of any nanoparticles (Figure 24). Due to the z-dependence in HAADF-STEM, the high density gold nanoparticles should appear as bright spots as in the case of the larger nanoparticles, but the inner matrix shows no bright spots in the present case.[74, 75] The mechanism of gold nanoparticles formation is assumed to be the oxidation of the Ni(II)macrocyclic species to Ni(III) in the framework. This is evidenced by the electron paramagnetic resonance (EPR) spectrum of the

resulting composite solid, which shows the anisotropic signals, $g_{\perp} = 2.142$ and $g_{\parallel} = 1.990$, characteristic for the tetragonally distorted Ni(III) species (Figure 25).[76, 77]

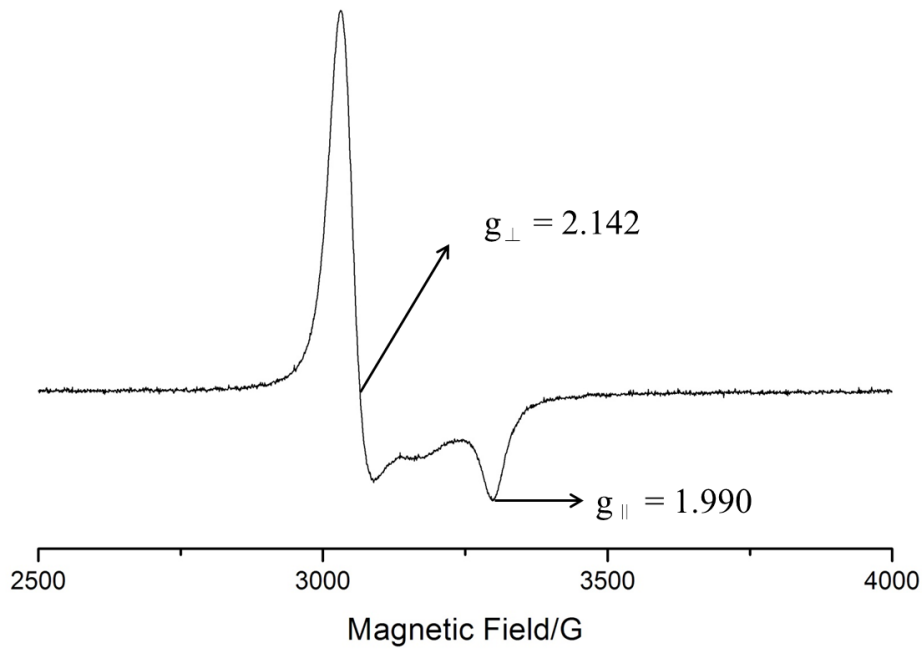

Figure 25. EPR spectrum for composite consisting of gold nanoparticles and **SNU-M55**, measured at frequency of 9.18263 GHz at 123K.

The effect of nanoparticle formation on the host is not clear, but PXRD patterns indicate that the framework structure of **SNU-M55** is altered by the formation of Au NPs as seen in Figure 26. The EDS spectrum also confirms that the host remains intact due to the nickel, and ruthenium peaks that appear in addition with the gold peak seen in Figure 27.

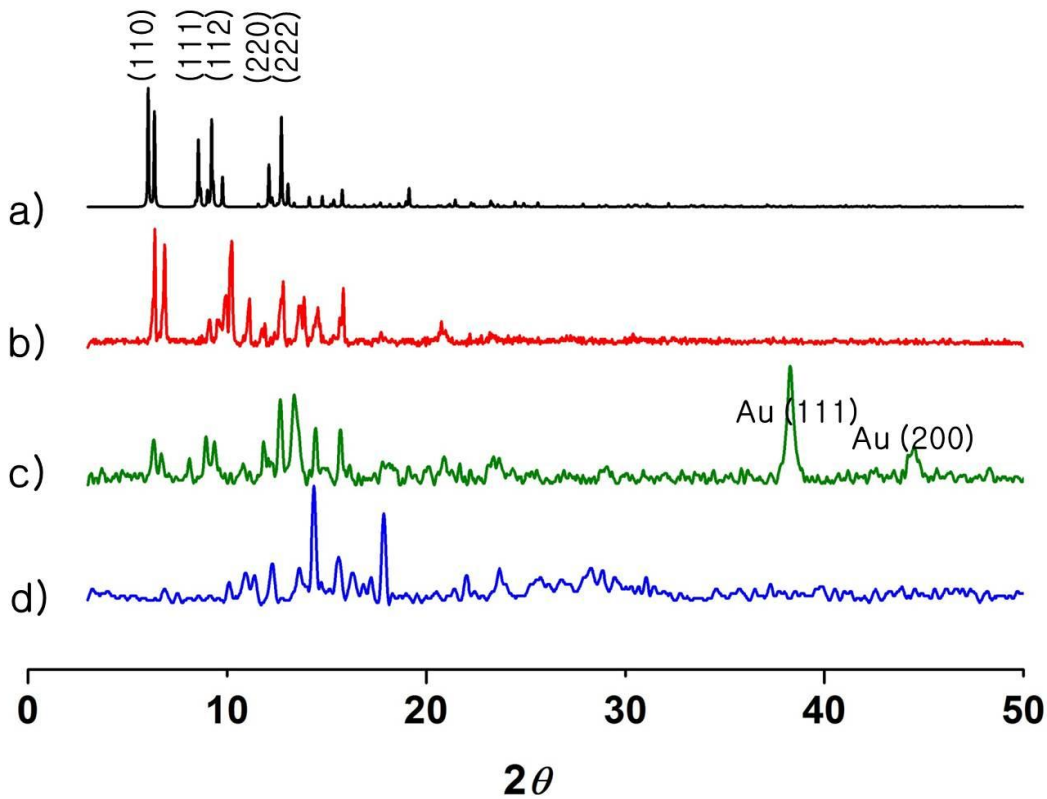

Figure 26. Powder X-ray diffraction patterns. a) The simulated PXRD pattern of **SNU-M55** derived from the single crystal X-ray data**.** b) **SNU-M55** as synthesized. c) Au NP and **SNU-M55** nanocomposite. d) Pt NP and **SNU-M55** nanocomposite.

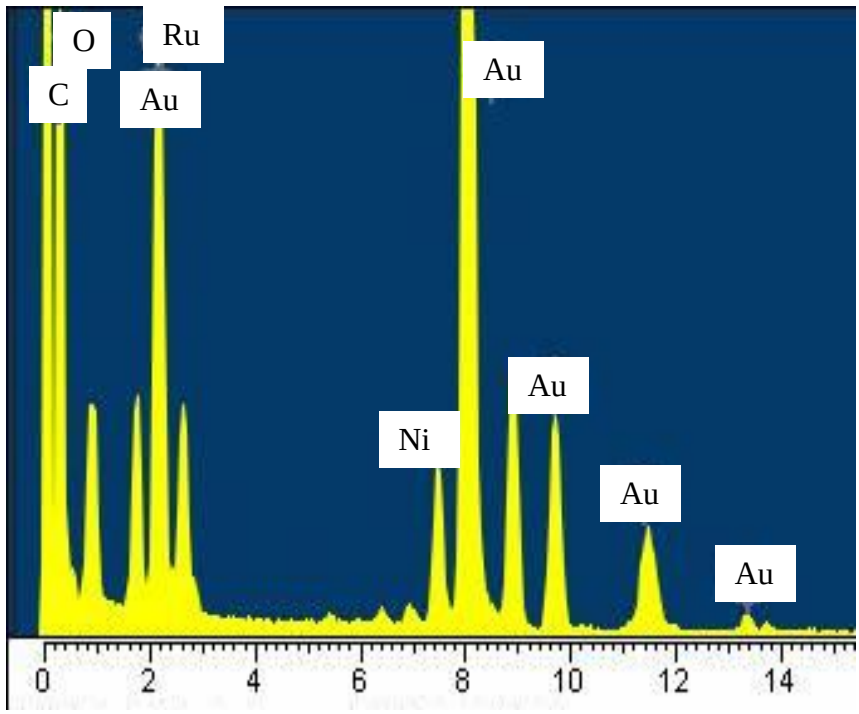

Figure 27. EDS spectrum of the gold nanoparticle MOF composite.

The formation of gold nanoparticles by the reaction with a redox-active MOF in this study is not a new finding, but the formation of shaped gold nanoparticles is particularly novel as it has never been previously observed. The formation of the shaped gold nanoparticles is believed to be a direct result of the light sensitizing $Ru(bpydc)_3^{2+}$ moiety. Previous studies have shown that ultraviolet irradiation can result in the formation of shaped gold nanoparticles.[59] Although previous studies used UV irradiation of a gold precursor in an aqueous solution together with a capping agent (polyvinyl alcohol), this particular method is capable of synthesizing shaped particles without the aid of a surfactant. Based on the previously proposed mechanism, it is suggested that even without a capping agent, ambient visible light irradiation can result in crystals with a preferential growth direction along the

Au(111) plane, which is supported by the d-spacing value. The growth mechanism of the shaped gold NPs has also been clarified by the Kossel-Stranski theory of face selective growth of crystals.[78]

III.2.2 Platinum Nanoparticles.

Platinum nanoparticles formed in a monodispersed fashion with sizes ranging 1.8 - 2.5 nm (Figure 28). The d-spacing value was found to be 2.225 Å in HRTEM (ICDD PDF no. 00-004-0802 d = 2.226 Å Pt). In the case of the platinum nanoparticles, due to the destruction of the framework during the formation of platinum nanoparticles as indicated by the PXRD patterns (Figure 26). It is proposed that the particles are supported on the remaining destroyed host solid. This is evidenced by elemental analysis data indicating that the Pt NPs are deposited in some decomposed form of the original host, which contains carbon, nitrogen and hydrogen. The EDS spectrum also supports the assertion that the framework is destroyed due to the lack of a ruthenium peak in the spectrum (Figure 29).

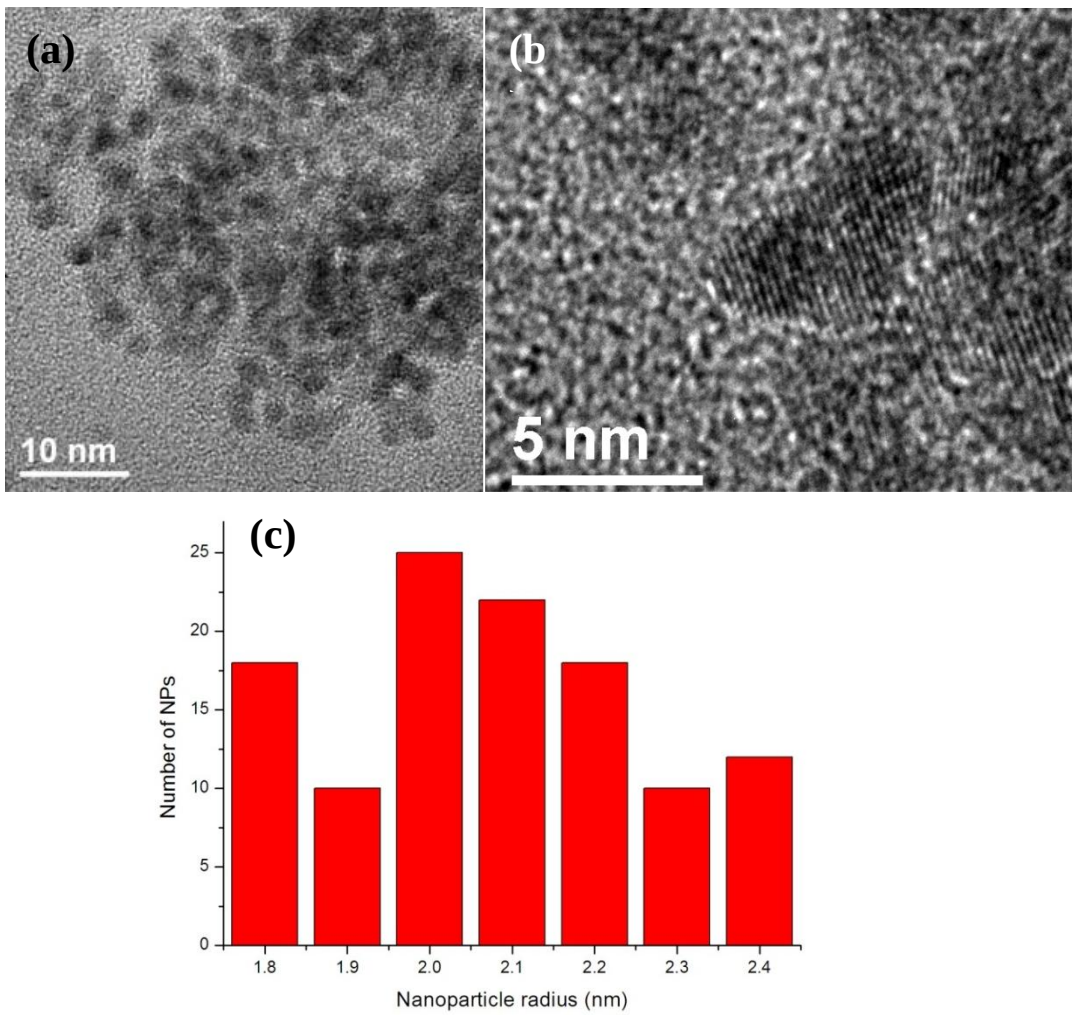

Figure 28. (a) HRTEM image of the platinum nanoparticles formed by **SNU-M55**. (b) A zoomed in image of the same sample showing the lattice fringes of the platinum nanoparticles. (c) A histogram of the size distribution of the platinum nanoparticles formed.

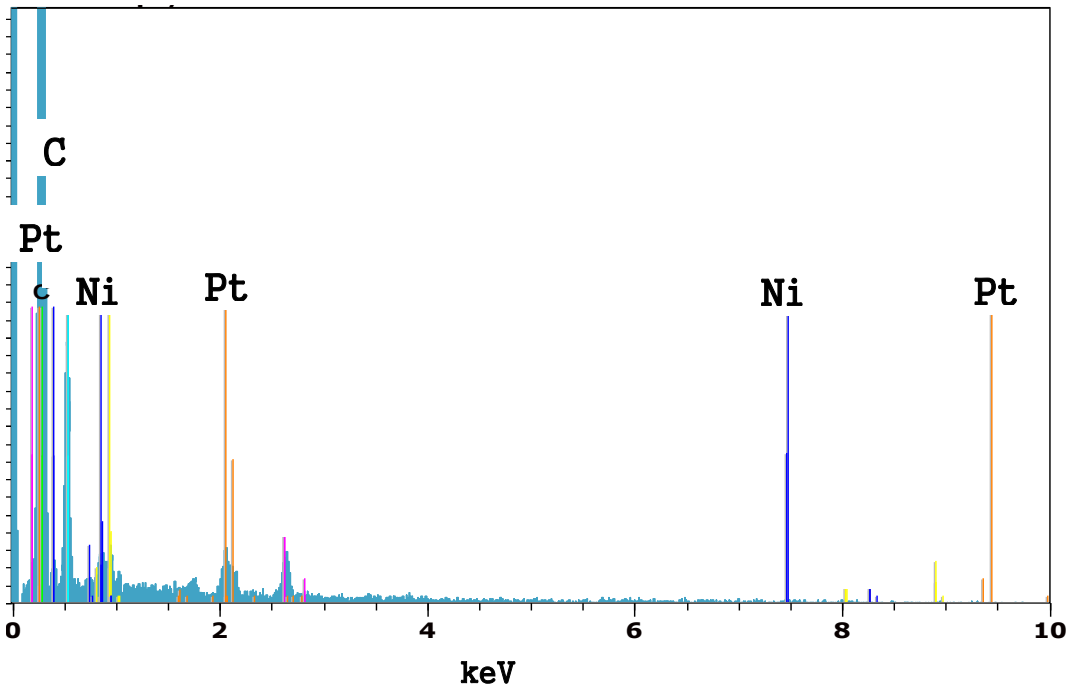

Figure 29. EDS spectrum of the platinum nanoparticles formed by **SNU-M55**.

The mechanism of platinum nanoparticle formation is unclear, but due to the EPR spectrum showing the absence of the Ni(III) macrocyclic species (Figure 30), it is assumed that nickel stays in a +2 oxidation state and the $Ru(bpydc)_3^{2+}$ moiety is responsible for the reduction of the platinum precursor to the observed platinum nanoparticles. We propose that the photoactive $Ru(bpydc)_3^{2+}$ moiety is promoted to a photo-excited state and reductively quenched by the framework, resulting in the strongly reducing Ru(I) species, which then reduces the Pt(II) precursor to elemental Pt (Scheme 3).[79] It is also presumed that this photoredox reaction breaks down the host framework and results in the $Ru(bpydc)_3^{2+}$ to go into the aqueous solution that contains the precursor and the host framework during the immersion procedure. The EDS spectra (Figure 29) indicates the absence of ruthenium in the

sample of platinum nanoparticles. The decomposition of the framework and the solvation of the liberated $Ru(bpydc)_3^{2+}$ unit are further supported by the absorption spectrum measured for the filtrate solution resulting from the immersion of **SNU-M55** in the platinum precursor solution, which shows a λ_{max} = 485 nm (Figure 31). The λ_{max} value is in close agreement with the previously reported value of 483 nm for the aqueous solution of $Ru(bpydc)_3^{2+}$.[79]

In order to test the catalytic activity of the platinum nanoparticles, the resulting composite was immersed in various buffer solutions with varying pH values and irradiated with a solar light simulator in an effort to reduce water into hydrogen gas. Despite the various combinations of electron relays, sacrificial electron donors and pH values, no evolution of hydrogen was observed.

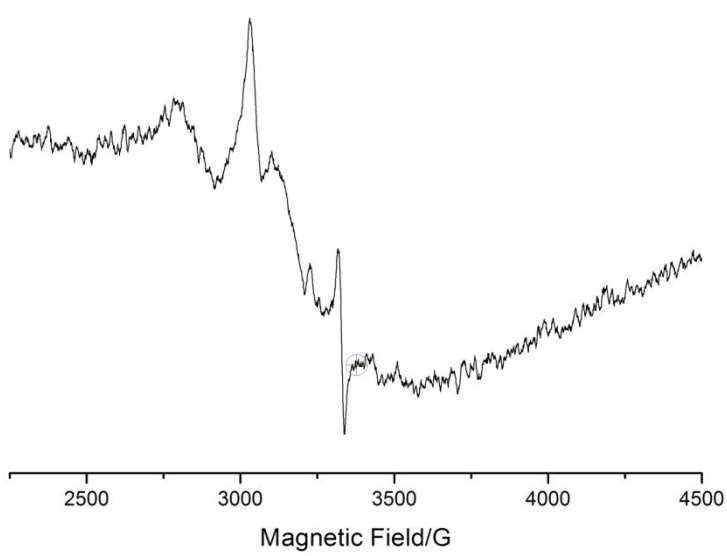

Figure 30. EPR spectrum for the platinum nanoparticles supported on the remaining destroyed **SNU-M55** solid measured at frequency of 9.18263 GHz at 123K.

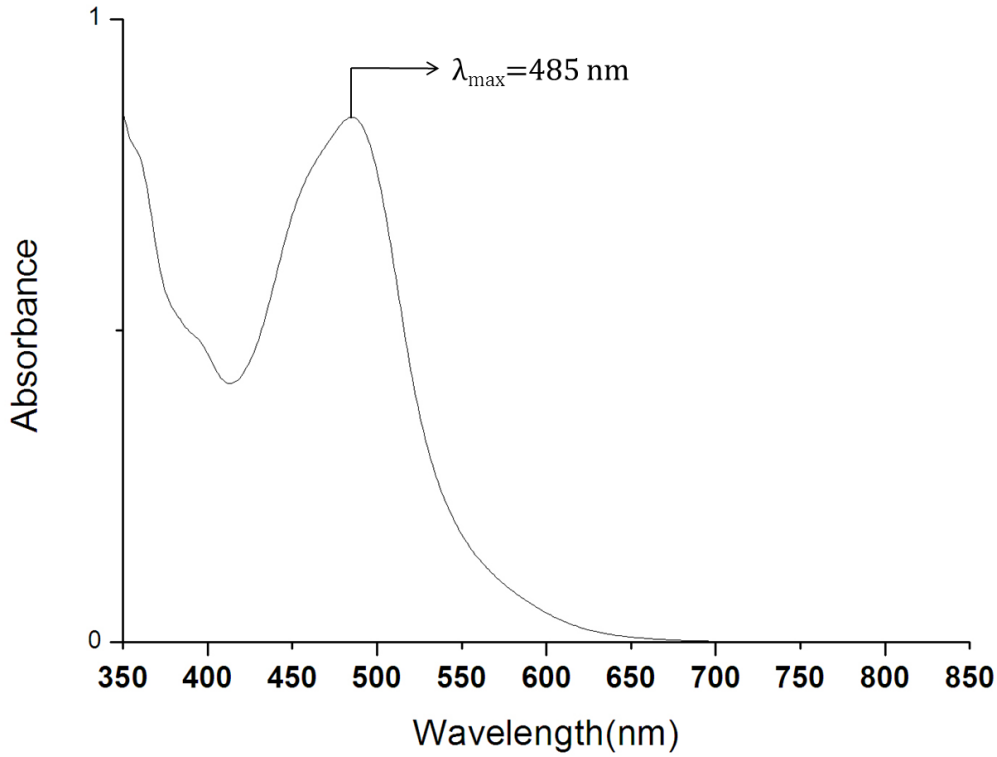

Figure 31. UV/Vis spectrum of filtrate resulting from immersion of **SNU-M55** in the aqueous solution (5 mL) of K_2PtCl_4 (34 mM) for 10 min.

.

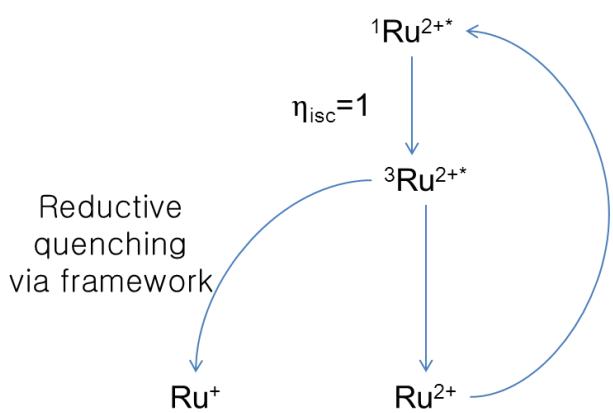

Scheme 3. The proposed mechanism for the reduction of K_2PtCl_4 by **SNU-M55**

III.3. A Comparative Study using [Ni(cyclam)(bpydc)]·5H_2O and the Molecular Building Blocks of SNU-M55 in the Formation of Au and Pt Nanoparticles.

In order to further elucidate the possible redox pathway and the effect of the $Ru(bpydc)_3^{2+}$ in the formation of gold and platinum nanoparticles, a previously reported[80] similar framework was synthesized. This particular framework is constructed of a monomacrocyclic Ni(II) ligand and the same organic building block used in **SNU-M55** (Figure 32). The analogue was treated with the exact same reaction conditions: immersing in an aqueous solution (5 mL, 34 mM) of a metal salt ($NaAuCl_4$•$6H_2O$, K_2PtCl_4) for 10 minutes.

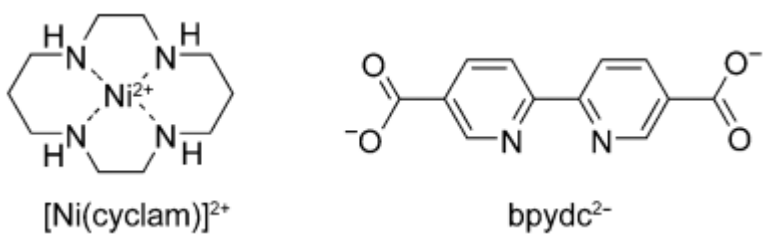

Figure 32. The building blocks used to construct the analogue of **SNU-M55.**

TEM imaging revealed that circular gold nanoparticles were formed while platinum nanoparticles were not (Figure 33). This finding supports the previously proposed mechanism of Ni(II) being oxidized to Ni(III) in the formation of gold particles. Furthermore it is clear that the light sensitizing $Ru(bpy)_3^{2+}$ moiety plays a crucial role in the synthesis of shaped nanoparticles. The proposed pathway for platinum nanoparticle formation using **SNU-M55** is also supported by this finding. Due to the lack of the $Ru(bpy)_3^{2+}$ in the analogue, it may be assumed that it is necessary in order to form platinum nanoparticles from a macrocyclic based MOF.

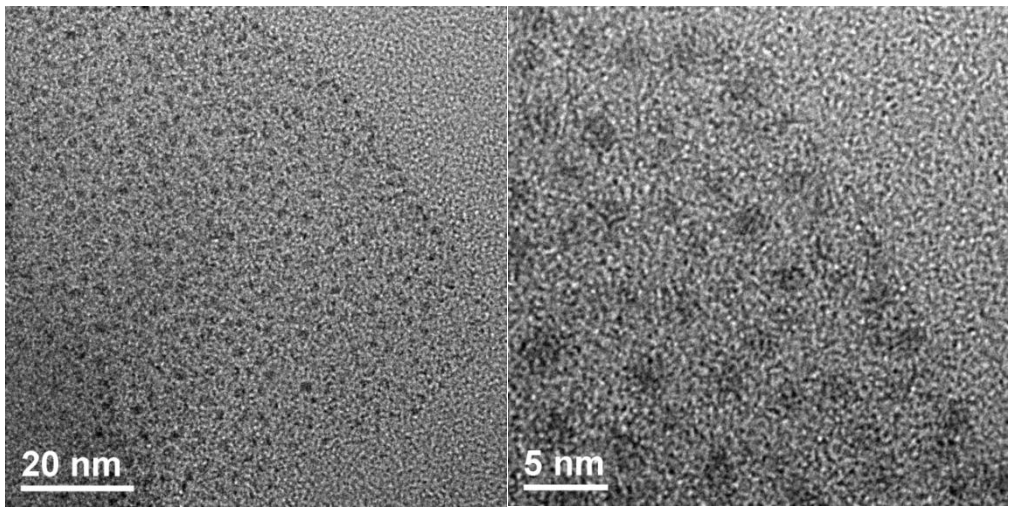

Figure 33. HRTEM image of the gold nanoparticles formed by [Ni(cyclam)(bpydc)]·5H_2O.

The molecular building blocks: Na_2bpydc, $[Ni_2(C_{26}H_{52}N_{10})Cl_4]\cdot H_2O$, and $RuCl_2(DMSO)_4$ were also mixed in the respective metal precursor solutions under the identical reaction conditions of **SNU-M55**, only to result in no formation of either metal nanoparticle.

IV. Conclusion

The ubiquitous nature of MOFs is attributed to the porous nature of the material which provides a robust platform that can be altered based on the molecular building blocks used. By using a bismacrocylcic based building block with a carboxylate based building block a redox active framework, **SNU-M55** was synthesized. This framework was capable of synthesizing shaped Au NPs and Pt NPs using the solution impregnation technique with aqueous solutions of the corresponding metal salts. The Ni(II) bismacrocyclic complex as well as the $Ru(bpydc)_3^{2+}$ center, were found to play key roles in the synthesis of both the shaped gold nanoparticles and platinum nanoparticles. Notably, these particles were also fabricated without the use of any additional reducing agent or surfactant. A mechanism for the formation of such nanoparticles based on the experimental evidences was also proposed. Although the framework is destroyed upon the formation of Pt NPs, this method still presents a facile process for the synthesis of metal nanoparticles. The test of catalytic activity of Pt NPs also failed to evolve any hydrogen gas from water.

Supporting Information

Table S1. Bond lengths (Å) and angles (°) of **SNU-M55.**

O(1)-C(15)	1.233(9)	Ru(1)-N(5)#4	2.042(5)
O(1)-Ni(2)	2.155(5)	Ru(1)-N(10)	2.071(6)
C(14)-N(5)	1.349(8)	Ru(1)-N(10)#4	2.071(6)
C(14)-C(17)	1.383(9)	Ru(1)-N(9)#4	2.079(6)
O(3)-C(16)	1.277(9)	Ni(2)-N(2)	2.063(8)
O(3)-Ni(2)	2.139(5)	Ni(2)-N(4)	2.058(7)
O(4)-C(16)	1.212(11)	Ni(2)-N(3)	2.053(11)
C(13)-C(12)	1.391(9)	Ni(2)-N(1)	2.061(10)
C(13)-N(5)	1.393(9)	N(2)-C(8)	1.470(19)
C(13)-C(18)#1	1.499(9)	N(2)-C(7)	1.46(2)
C(11)-C(17)	1.342(12)	N(4)-C(3)	1.425(15)
C(11)-C(12)	1.377(10)	N(4)-C(5)	1.456(15)
O(2)-C(15)	1.201(11)	N(1)-C(4)	1.499(19)
C(15)-C(17)	1.568(10)	N(3)-C(1)	1.50(2)
C(16)-C(20)	1.511(9)	N(3)-C(6)	1.464(18)
N(5)-Ru(1)	2.042(5)	C(3)-N(8)	1.391(18)
C(21)-N(10)#2	1.363(8)	C(6)-C(7)	1.55(3)
C(21)-C(20)	1.408(11)	C(9)-C(8)	1.51(3)
C(20)-C(22)	1.390(10)	C(5)-C(4)	1.51(2)
C(18)-C(19)	1.335(12)	N(8)-C(1)	1.49(2)
C(18)-N(10)#2	1.349(8)	N(10)-C(18)#1	1.349(8)
C(18)-C(13)#2	1.499(9)	N(10)-C(21)#1	1.363(8)
C(22)-C(19)	1.385(12)	C(78)-O(77)	0.49(13)
C(23)-N(8)	1.483(16)	C(78)-O(55)	1.42(11)
C(23)-C(24)	1.52(2)	C(78)-C(34)	1.79(11)
C(24)-C(25)	1.28(3)	C(67)-C(67)#4	1.70(3)
C(24)-C(29)	1.46(2)	C(67)-C(66)	1.80(2)
C(10)-C(9)	1.42(3)	C(67)-C(33)	2.01(2)
C(10)-N(1)	1.47(2)	C(33)-C(34)	1.33(3)
C(25)-C(29)#3	1.38(3)	C(33)-C(55)	1.86(3)
C(29)-C(25)#3	1.38(3)	C(34)-C(55)	1.12(3)
N(9)-C(33)	1.218(18)	C(34)-O(77)	1.74(4)
N(9)-C(67)	1.242(18)	C(66)-C(55)	1.04(2)
N(9)-Ru(1)	2.079(6)		

Infrared Spectra of Products

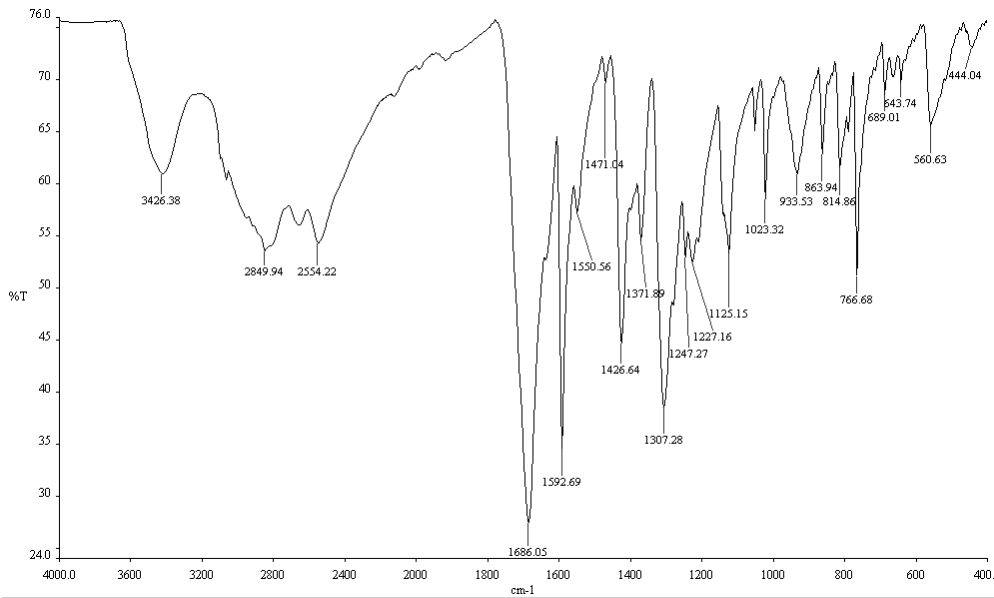

Figure S1. Infrared spectrum of BpyDC ligand.

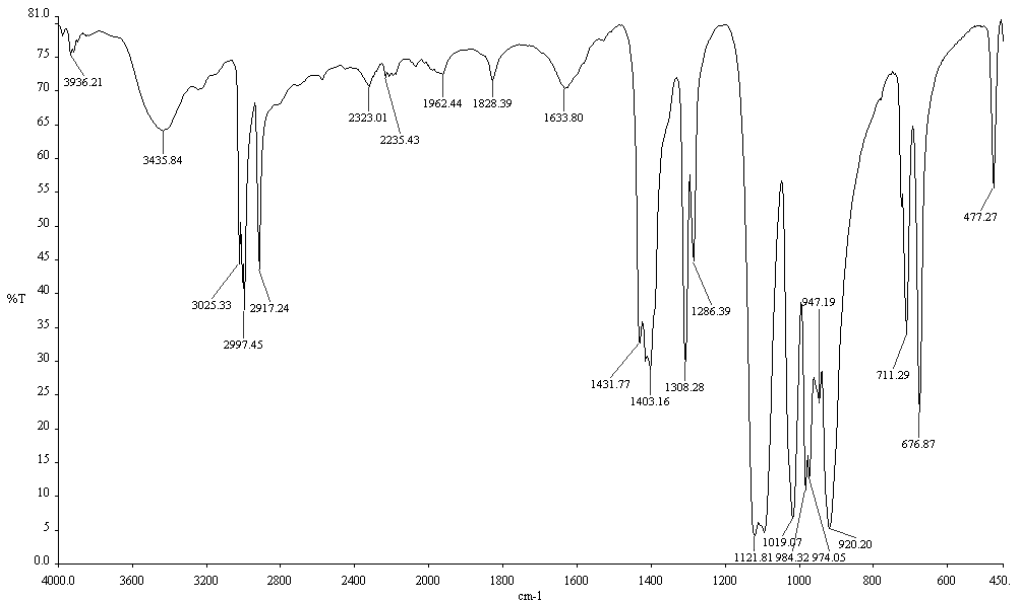

Figure S2. Infrared spectrum of $Ru(DMSO)_4Cl_2$.

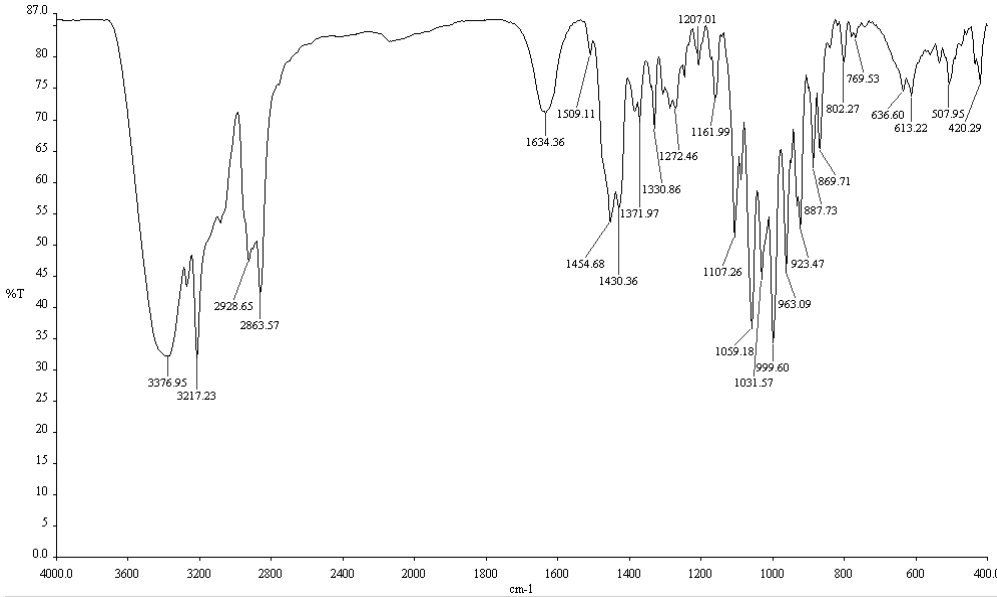

Figure S3. Infrared spectrum of $[Ni_2(C_{26}H_{52}N_{10})Cl_4]\cdot H_2O$ (bismacrocycle).

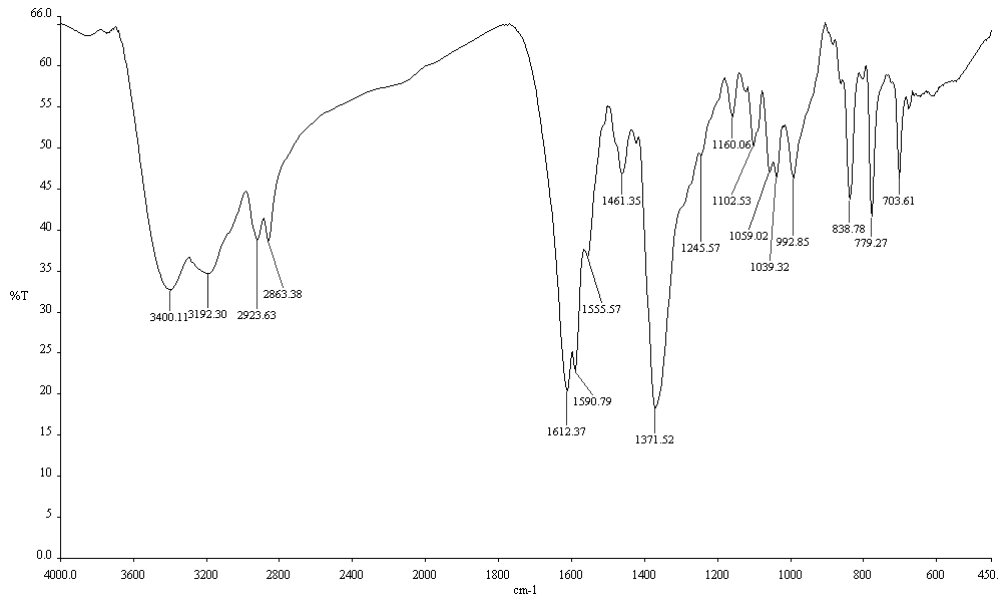

Figure S4. Infrared spectrum of **SNU-M55**.

References

1. J. R. Long and O. M. Yaghi, *Chem. Soc. Rev.*, 2009, **38**, 1213-1214.
2. H.-C. Zhou, J. R. Long and O. M. Yaghi, *Chem. Rev.*, 2012, **112**, 673-674.
3. B. F. Hoskins and R. Robson, *J. Am. Chem. Soc.*, 1989, **111**, 5962-5964.
4. B. F. Hoskins and R. Robson, *J. Am. Chem. Soc.*, 1990, **112**, 1546-1554.
5. S. M. Cohen, *Chem. Rev.*, 2011, **112**, 970-1000.
6. O. M. Yaghi, M. O'Keeffe, N. W. Ockwig, H. K. Chae, M. Eddaoudi and J. Kim, *Nature*, 2003, **423**, 705-714.
7. H. Li, M. Eddaoudi, M. O'Keeffe and O. M. Yaghi, *Nature*, 1999, **402**, 276-279.
8. M. Eddaoudi, J. Kim, N. Rosi, D. Vodak, J. Wachter, M. O'Keeffe and O. M. Yaghi, *Science*, 2002, **295**, 469-472.
9. J. L. C. Rowsell, A. R. Millward, K. S. Park and O. M. Yaghi, *J. Am. Chem. Soc.*, 2004, **126**, 5666-5667.
10. H. K. Chae, D. Y. Siberio-Perez, J. Kim, Y. Go, M. Eddaoudi, A. J. Matzger, M. O'Keeffe and O. M. Yaghi, *Nature*, 2004, **427**, 523-527.
11. D. J. Tranchemontagne, J. L. Mendoza-Cortes, M. O'Keeffe and O. M. Yaghi, *Chem. Soc. Rev.*, 2009, **38**, 1257-1283.
12. R. Mahesh Kumar and V. Subramanian, *Int. J. Hydrogen Energy*, 2011, **36**, 10737-10747.
13. R. J. Kuppler, D. J. Timmons, Q.-R. Fang, J.-R. Li, T. A. Makal, M. D. Young, D. Yuan, D. Zhao, W. Zhuang and H.-C. Zhou, *Coord. Chem. Rev.*, 2009, **253**, 3042-3066.

14. H. J. Choi and M. P. Suh, *J. Am. Chem. Soc.*, 1998, **120**, 10622-10628.

15. M. P. Suh, Y. E. Cheon and E. Y. Lee, *Coord. Chem. Rev.*, 2008, **252**, 1007-1026.

16. K. Sumida, D. L. Rogow, J. A. Mason, T. M. McDonald, E. D. Bloch, Z. R. Herm, T.-H. Bae and J. R. Long, *Chem. Rev.*, 2011, **112**, 724-781.

17. X.-S. Wang, S. Ma, P. M. Forster, D. Yuan, J. Eckert, J. J. López, B. J. Murphy, J. B. Parise and H.-C. Zhou, *Angew. Chem. Int. Ed.*, 2008, **47**, 7263-7266.

18. M. P. Suh, H. J. Park, T. K. Prasad and D.-W. Lim, *Chem. Rev.*, 2011, **112**, 782-835.

19. H. J. Park, D.-W. Lim, W. S. Yang, T.-R. Oh and M. P. Suh, *Chem.-Eur. J.*, 2011, **17**, 7251-7260.

20. E. Y. Lee, S. Y. Jang and M. P. Suh, *J. Am. Chem. Soc.*, 2005, **127**, 6374-6381.

21. H. J. Park and M. P. Suh, *Chem.-Eur. J.*, 2008, **14**, 8812-8821.

22. J. Lee, O. K. Farha, J. Roberts, K. A. Scheidt, S. T. Nguyen and J. T. Hupp, *Chem. Soc. Rev.*, 2009, **38**, 1450-1459.

23. M. Fujita, Y. J. Kwon, S. Washizu and K. Ogura, *J. Am. Chem. Soc.*, 1994, **116**, 1151-1152.

24. R.-Q. Zou, H. Sakurai and Q. Xu, *Angew. Chem. Int. Ed.*, 2006, **45**, 2542-2546.

25. Y. K. Hwang, D.-Y. Hong, J.-S. Chang, S. H. Jhung, Y.-K. Seo, J. Kim, A. Vimont, M. Daturi, C. Serre and G. Férey, *Angew. Chem. Int. Ed.*, 2008, **47**, 4144-4148.

26. C. Wang, K. E. deKrafft and W. Lin, *J. Am. Chem. Soc.*, 2012, **134**, 7211-7214.

27. M. Meilikhov, K. Yusenko, D. Esken, S. Turner, G. Van Tendeloo and R. A. Fischer, *Eur. J. Inorg. Chem.*, 2010, **2010**, 3701-3714.

28. A. Dhakshinamoorthy and H. Garcia, *Chem. Soc. Rev.*, 2012, **41**, 5262-5284.

29. S. Proch, J. Herrmannsdörfer, R. Kempe, C. Kern, A. Jess, L. Seyfarth and J. Senker, *Chem.-Eur. J.*, 2008, **14**, 8204-8212.

30. S. Opelt, S. Türk, E. Dietzsch, A. Henschel, S. Kaskel and E. Klemm, *Catal. Commun.*, 2008, **9**, 1286-1290.

31. Y. E. Cheon and M. P. Suh, *Chem.-Eur. J.*, 2008, **14**, 3961-3967.

32. Y. E. Cheon and M. P. Suh, *Angew. Chem. Int. Ed.*, 2009, **48**, 2899-2903.

33. H. R. Moon, D.-W. Lim and M. P. Suh, *Chem. Soc. Rev.*, 2013, **42**, 1807-1824.

34. S. Hermes, M.-K. Schröter, R. Schmid, L. Khodeir, M. Muhler, A. Tissler, R. W. Fischer and R. A. Fischer, *Angew. Chem. Int. Ed.*, 2005, **44**, 6237-6241.

35. D. Esken, S. Turner, O. I. Lebedev, G. Van Tendeloo and R. A. Fischer, *Chem. Mater.*, 2010, **22**, 6393-6401.

36. D.-W. Lim, J. W. Yoon, K. Y. Ryu and M. P. Suh, *Angew. Chem. Int. Ed.*, 2012, **51**, 9814-9817.

37. R. J. T. Houk, B. W. Jacobs, F. E. Gabaly, N. N. Chang, A. A. Talin, D. D. Graham, S. D. House, I. M. Robertson and M. D. Allendorf, *Nano Lett.*, 2009, **9**, 3413-3418.

38. T. Ishida, M. Nagaoka, T. Akita and M. Haruta, *Chem.-Eur. J.*, 2008, **14**, 8456-8460.

39. M. S. El-Shall, V. Abdelsayed, A. E. R. S. Khder, H. M. A. Hassan, H. M. El-Kaderi and T. E. Reich, *J. Mater. Chem.*, 2009, **19**, 7625-7631.

40. H. R. Moon, J. H. Kim and M. P. Suh, *Angew. Chem. Int. Ed.*, 2005, **44**, 1261-1265.

41. M. P. Suh, H. R. Moon, E. Y. Lee and S. Y. Jang, *J. Am. Chem. Soc.*, 2006, **128**, 4710-4718.

42. S. Chen and Y. Yang, *J. Am. Chem. Soc.*, 2002, **124**, 5280-5281.

43. M.-C. Daniel and D. Astruc, *Chem. Rev.*, 2003, **104**, 293-346.

44. M. A. El-Sayed, *Acc. Chem. Res.*, 2001, **34**, 257-264.

45. A. M. Funston, D. E. Gómez, M. Karg, K. C. Vernon, T. J. Davis and P. Mulvaney, *The Journal of Physical Chemistry Letters*, 2013, 1994-2001.

46. R. Elghanian, J. J. Storhoff, R. C. Mucic, R. L. Letsinger and C. A. Mirkin, *Science*, 1997, **277**, 1078-1081.

47. C. P. Collier, R. J. Saykally, J. J. Shiang, S. E. Henrichs and J. R. Heath, *Science*, 1997, **277**, 1978-1981.

48. S. J. Lee, S. W. Han, H. J. Choi and K. Kim, *The Journal of Physical Chemistry B*, 2002, **106**, 2892-2900.

49. A. Pal, S. Shah and S. Devi, *Mater. Chem. Phys.*, 2009, **114**, 530-532.

50. T. Itakura, K. Torigoe and K. Esumi, *Langmuir*, 1995, **11**, 4129-4134.

51. V. G. Pol, D. N. Srivastava, O. Palchik, V. Palchik, M. A. Slifkin, A. M. Weiss and A. Gedanken, *Langmuir*, 2002, **18**, 3352-3357.

52. R. M. Stiger, S. Gorer, B. Craft and R. M. Penner, *Langmuir*, 1998, **15**,

790-798.

53. M. Grzelczak, J. Perez-Juste, P. Mulvaney and L. M. Liz-Marzan, *Chem. Soc. Rev.*, 2008, **37**, 1783-1791.

54. M. Min, C. Kim and H. Lee, *J. Mol. Catal. A: Chem.*, 2010, **333**, 6-10.

55. K. Saha, S. S. Agasti, C. Kim, X. Li and V. M. Rotello, *Chem. Rev.*, 2012, **112**, 2739-2779.

56. K. Mallick, Z. L. Wang and T. Pal, *J. Photochem. Photobiol., A*, 2001, **140**, 75-80.

57. H.-L. Wu, C.-H. Kuo and M. H. Huang, *Langmuir*, 2010, **26**, 12307-12313.

58. M. R. Langille, M. L. Personick, J. Zhang and C. A. Mirkin, *J. Am. Chem. Soc.*, 2012, **134**, 14542-14554.

59. Y. Zhou, C. Y. Wang, Y. R. Zhu and Z. Y. Chen, *Chem. Mater.*, 1999, **11**, 2310-2312.

60. F. Raimondi, G. G. Scherer, R. Kötz and A. Wokaun, *Angew. Chem. Int. Ed.*, 2005, **44**, 2190-2209.

61. K. Yamauchi, S. Masaoka and K. Sakai, *Dalton Trans.*, 2011, **40**, 12447-12449.

62. L. D. Rampino and F. F. Nord, *J. Am. Chem. Soc.*, 1941, **63**, 2745-2749.

63. R. Rafaeloff, Y. Haruvy, J. Binenboym, G. Baruch and L. A. Rajbenbach, *J. Mol. Catal.*, 1983, **22**, 219-233.

64. M. Zhao and R. M. Crooks, *Angew. Chem. Int. Ed.*, 1999, **38**, 364-366.

65. H. J. Choi and M. P. Suh, *J. Am. Chem. Soc.*, 2004, **126**, 15844-15851.

66. C. Janiak, S. Deblon, H.-P. Wu, M. J. Kolm, P. Klüfers, H. Piotrowski and P. Mayer, *Eur. J. Inorg. Chem.*, 1999, **1999**, 1507-1521.

67. I. P. Evans, A. Spencer and G. Wilkinson, *Journal of the Chemical Society, Dalton Transactions*, 1973, 204-209.

68. Z. Otwinowsky and W. Minor, *Processing of X-ray Diffraction Data Collected in Oscillation Mode, Methods in Enzymology* (Eds.: C. W. Carter, R. M. Sweet),A. Press:New York (USA), **1996**, 276, 307-326

69. G. M. Sheldrick, *Acta Crystallogr., Sect. A: Found. Crystallogr.*, 2008, **A46**, 112-122.

70. G. M. Sheldrick, *Acta Crystallogr.* , **2008**,*A46*,112-122

71. A. Spek, *J. Appl. Crystallogr.*, 2003, **36**, 7-13.

72. R. J. Crutchley and A. B. P. Lever, *Inorg. Chem.*, 1982, **21**, 2276-2282.

73. R. J. P. Williams, *Journal of the Chemical Society (Resumed)*, 1955, **0**, 137-145.

74. C. Kübel, A. Voigt, R. Schoenmakers, M. Otten, D. Su, T.-C. Lee, A. Carlsson and J. Bradley, *Microsc. Microanal.*, 2005, **11**, 378-400.

75. M. Müller, S. Turner, O. I. Lebedev, Y. Wang, G. van Tendeloo and R. A. Fischer, *Eur. J. Inorg. Chem.*, 2011, **2011**, 1876-1887.

76. M. P. Suh, E. Y. Lee and B. Y. Shim, *Inorg. Chim. Acta*, 1998, **269**, 337-341.

77. M. P. Suh, in *Adv. Inorg. Chem.*, ed. A. G. Sykes, Academic Press, 1996, vol. Volume 44, pp. 93-146.

78. B. Brüche, *Kolloid-Zeitschrift*, 1960, **170**, 97-104.

79. M. K. Nazeeruddin and K. Kalyanasundaram, *Inorg. Chem.*, 1989, **28**, 4251-4259.

80. E. Y. Lee and M. P. Suh, *Angew. Chem. Int. Ed.*, 2004, **43**, 2798-2801.

Acknowledgments

I would like to begin with thanking my undergraduate advisors, Professor Sunhee Choi and Professor James A. Larrabee at Middlebury College, who gave me both the encouragement and sound foundation in chemistry that has allowed me to complete this degree. Their continued guidance and support have been invaluable over the past decade.

I would like to continue by thanking my current advisor, Professor Myunghyun Paik Suh, who has supported and given me a deep appreciation for the beauty of chemistry and its applications. Her energy and diligence will be a constant motivator in the future.

Lastly, I would like to thank all of my labmates, Hye Jeong Park, Daeho Hong, Daewoon Lim, Seyong Kim, Myung-ho Choi, Siyoung Sung, Thazhe Kootteri Prasad, and Lin-Hua Xie for their help and friendship during my time here at Seoul National University.